

Additive Manufacturing with Stellite 6 Metal-cored Wire  
by Gas Tungsten Arc Welding and Plasma Arc Welding  
Methods

by

Shahryar Sahrhiri Fard, B. Eng.

A thesis submitted to the Faculty of Graduate and Postdoctoral  
Affairs in partial fulfillment of the requirements for the degree of

Master of Applied Sciences

in

Mechanical Engineering

Carleton University  
Ottawa, Ontario

© 2021, Shahryar Shahryari Fard

## **Abstract**

Metal-cored wires offer an opportunity to manufacture highly alloyed materials in the form of a tubular wire which may include any compatible powder alloy. These wires can be used with Wire and Arc Additive Manufacturing methods such as Gas Tungsten Arc Welding (GTAW) and Plasma Arc Welding (PAW). These methods use a lower cost, and less complex heat source compared with Laser and Electron-Beam Processes. In this study, Stellite 6 metal-cored wire was utilized with GTAW to determine printing parameters. However, initial experiment showed that manufacturing thin walls with <3.5 mm thickness would not be possible with continuous weld beads, resulting in poor repeatability and geometrical defects. Therefore, the Coordinated Heat and Feed (CHF) printing strategy was developed and validated to address these issues. Furthermore, a PAW system was adopted in place of GTAW for an increased flexibility. However, preliminary tests performed with the CHF method resulted in high amount of oxidation although the geometrical features were improved.

## **Acknowledgements**

A lot of people have helped me for completion of this research, and the personal and professional growth involved. My supervisors, Dr. Hanspeter Frei and Dr. Xiao Huang, have provided me with support, knowledge, and most importantly, the freedom to discover, to express, and to enjoy my work.

I am grateful for the help and support from the following staff and colleagues at Carleton University: Alex Proctor, James Cann, David Raude, Kevin Sangster, Steve Truttmann, Aric Adcock, Wei Wang, Malcolm Dinovitzer, Dr. Jianqun Wang, Dr. John Goldak, Dr. Bingjie Xiao, and Adria Barcelo Singh. I extend my gratitude to Dr. Matthew Yaw at Kennametal Stellite Inc. for his support and contributions to my project.

I thank my friends and family, especially my parents and brother, for their loving encouragements and comforting me during difficult times. Finally, thank you Mahdokht for making my days better and better.

I dedicate this thesis to my late uncle, Kaykhosrow Shahryari Fard, for all our memories and for everything he had done for me.

# Table of Contents

<b>Abstract</b> .....	<b>ii</b>
<b>Acknowledgements</b> .....	<b>iii</b>
<b>Table of Contents</b> .....	<b>iv</b>
<b>List of Tables</b> .....	<b>viii</b>
<b>List of Figures</b> .....	<b>ix</b>
<b>Preface</b> .....	<b>1</b>
<b>Acronyms</b> .....	<b>2</b>
<b>Chapter 1: Introduction</b> .....	<b>3</b>
1.1    Motivation .....	3
1.2    Objective.....	3
1.3    Thesis Overview .....	4
<b>Chapter 2: Literature Review</b> .....	<b>6</b>
2.1    Metal Additive Manufacturing .....	6
2.1.1    Metal-AM in Aerospace.....	6
2.1.2    Metal-AM in Biomedical Industry .....	8
2.2    Economics of Metal-AM.....	10
2.3    Types of Metal-AM: The Feed Stock Perspective .....	12
2.3.1    Powder Bed Systems.....	12
2.3.1.1    Selective Laser Melting (SLM) Selective Laser Sintering (SLS) .....	12
2.3.1.2    Electron Beam Melting (EBM) .....	13
2.3.2    Powder Feed Systems .....	14
2.3.2.1    Laser Engineered Net Shaping (LENS).....	14
2.3.3    Wire Feed Systems.....	15

2.3.3.1	Gas Metal Arc Welding Additive Manufacturing (GMAW-AM).....	16
2.3.3.2	Gas Tungsten Arc Welding Additive Manufacturing (GTAW-AM) .....	17
2.3.3.3	Plasma Arc Welding Additive Manufacturing (PAW-AM).....	18
2.4	Materials and Microstructure in Metal-AM .....	19
2.4.1	Superalloys.....	20
2.4.2	Stellite 6: A Co-based Superalloy .....	20
2.5	Advantages and Disadvantages of Metal-AM.....	21
<b>Chapter 3: Printer Modification and PAW Adoption.....</b>		<b>23</b>
3.1	The Wire: Ø1.2 mm Metal-Cored Stellite 6 Wire .....	23
3.2	The Printer .....	24
3.3	The Wire Feeding Mechanism .....	25
3.3.1	Shortcomings of the wire feeder .....	27
3.3.1.1	Defective Wire.....	27
3.3.1.2	Misalignment of the Wire and Power Source.....	28
3.3.1.3	Unwanted Wire Motion and Wire Slippage .....	30
3.4	Improvements to Gas Tungsten Arc Welding System .....	32
3.5	The Control System Upgrade on the Printer.....	35
3.6	Plasma Arc Welding (PAW) System Adoption .....	36
<b>Chapter 4: Coordinated Heat and Feed Printing Strategy for Wire and Arc Additive Manufacturing of Metal-Cored Wires .....</b>		<b>39</b>
4.1	Abstract .....	39
4.2	Introduction .....	40
4.3	Materials and Methods .....	42
4.3.1	Experimental Setup .....	42
4.3.2	Conventional GTAW-AM .....	44
4.3.3	Coordinated Heat and Feed Printing Strategy.....	45

4.4	Results and Discussion .....	48
4.4.1	Conventional GTAW-AM .....	48
4.4.2	Coordinated Heat and Feed Printing Strategy .....	51
4.4.3	Material Properties and Comparison of the Specimens .....	54
4.5	Conclusion.....	60
4.6	Acknowledgements .....	61
<b>Chapter 5: Investigation on WAAM of Stellite 6 Metal-cored Wire with PAW .....</b>		<b>62</b>
5.1	Introduction .....	62
5.2	Experimental Setup and Procedure.....	63
5.2.1	Experimental Setup: .....	63
5.2.2	Experimental Procedure .....	65
5.2.3	Preliminary Experiments.....	65
5.2.4	CHF Specimens.....	67
5.3	Results and Discussions .....	69
5.3.1	Preliminary Experiments.....	69
5.3.2	Oxidation Analysis.....	71
5.3.3	CHF Specimens.....	72
5.3.3.1	Geometrical Features.....	72
5.3.3.2	Microstructural Analysis .....	74
5.4	Conclusion.....	75
<b>Chapter 6: Conclusion and Future Work.....</b>		<b>77</b>
6.1	Gas Tungsten Arc Welding Additive Manufacturing.....	77
6.1.1	Equipment Setup and Preliminary Experiments .....	77
6.1.2	Coordinated Heat and Feed (CHF) Printing Strategy .....	77
6.1.3	CHF Validation .....	78
6.1.4	Future Work .....	78

6.2	Plasma Arc Welding Additive Manufacturing .....	79
6.2.1	Equipment Setup and Preliminary Experiments .....	79
6.2.2	CHF Printing Strategy.....	80
6.2.3	Future Work .....	80
	<b>References .....</b>	<b>81</b>
	Appendix A - Failed Square Printing .....	99

## List of Tables

Table 1: Some of the torch-wire configurations tested to GTAW system.....	33
Table 2: Composition of Stellite 6 metal-cored welding wire (wt.%) (Ref 22) .....	44
Table 3: 7-layer CFH specimen running parameters .....	48
Table 4: Composition of the defect and its surrounding on layer 5 of the CHF specimen	58
Table 5: Printing parameters the surface oxidation analysis. ....	67
Table 6: Printing parameters for the PAW-AM CHF samples. ....	68
Table 7: Average oxygen content (%wt.) of the samples based on the shades of grey on the surface of the beads in Figure 39a detected by EDX.....	71

## List of Figures

Figure 1: Antenna bracket redesign process [8] .....	7
Figure 2: GE9X turboprop engine and the heat exchanger that was additively manufactured resulting in lower weight, cost, and number of components [10].....	8
Figure 3: The Anatomy-Adaptive Titanium Mesh Cage designed for subsidence prevention. A-D, CAD model of the TMC. A-H, additively manufactured TMC [17]....	10
Figure 4: AM process map represented by Ding et al. [21] for the material jetting process. The steps provided in this map are common among the other AM processes.....	11
Figure 5: Diagram of a SLM powder bed system [25]. The laser is the power source for melting the 20-100um powder layer to build a component. ....	13
Figure 6: A system depicting the LENS process for Powder Feed Metal-AM system [32]. The powder is blown onto the area that is melted by the laser. ....	15
Figure 7: Schematic of the Gas Metal Arc Welding Additive Manufacturing setup [37]	16
Figure 8: Schematic of GTAW system which is shown to weld two pieces by adding the filler metal [40]. The consumable electrode can be a wire. ....	17
Figure 9: Heat input density of a vertical GTAW system measured by Nestor's water-cooled split anode copper plate [39]. ....	18
Figure 10: Schematic of PAW torch where the dark gray component is the plasma nozzle (not labeled by the reference) [41].....	19
Figure 11: a) Optical micrograph of cast Stellite 6 superalloy. b) SEM micrograph of cast Stellite 6. Both micrographs include the labels regarding the microstructure [53]. ....	21

Figure 12: Stellite 6 wire. (a) Image of the wire cross section. (b) Schematic of the perpendicular cross section of the wire. (c) Schematic of the lateral cross section of the wire. .... 23

Figure 13: The custom Computerized Numerical Control (CNC) machine for WAAM research at Carleton University..... 25

Figure 14: The Original Wire Feeding Mechanism. (a) indicates the overall setup where the wire goes through the wire feeder and the wire nozzle. (b) The Wire Feeder close-up photo where the arrow indicates rotation..... 26

Figure 15: Wire nozzle setup for the GTAW system. The setup is similar for the PAW system as well, the power source is perpendicular to the substrate and the wire is fed from an angle. .... 27

Figure 16: Examples of Wire and Arc Misalignment..... 29

Figure 17: An example of wire slippage. Bead 18 is shorter than Bead 19 even though the wire was cut similarly, and the beads were expected to begin at the same location, however, Bead 18 started about 1.5 mm after Bead 19 because of wire slippage inside the wire guide..... 30

Figure 18: The slack in the wire guide. (a) wire feeding setup where the wire feeder and the wire nozzle and holder are fixed, however, they move relative to each other. (b) and (c) relative wire position (yellow hatch) and wire guide (pink hatch) when the wire is slightly pushed in and out of the nozzle, respectively..... 31

Figure 19: The modified wire feeder location relative to the nozzle and holder. The wire guide (same spring) can be replaced with any rigid cylindrical tube to protect the wire. This setup can be utilized for both welding methods. .... 32

Figure 20: The notch that was added to the cup to restrict the motion of the wire..... 35

Figure 21: Conceptualization of the of the Printer interface with the PAW system..... 36

Figure 22: Torch holder and wire nozzle system designed for the PAW wire and arc additive manufacturing. The red arrow indicates the rotation of the torch along vertical axis. .... 37

Figure 23: PAW torch calibration which should be performed until the wire is at the center of the circular marks..... 38

Figure 24: Experimental setup for the WAAM research at Carleton University. The 3D printer is a custom build CNC machine with a computer-controlled wire feeder. The travel speed and direction, the welding current, and the wire feed are controlled independently. .... 43

Figure 25: Computer rendered schematic showing weld pool formation, the first step of the CHF deposition process and the related terminologies..... 46

Figure 26: The illustration of the Coordinated Heat and Feed (CHF) printing strategy for Stellite 6. a) Behavior of the current and wire feed rate for two consecutive path segments. b) – e) Schematic of the wire, weld pool, and the deposits according to the label on a). .... 47

Figure 27: Single layer beads using the conventional GTAW-AM method with identical printing parameters for all the trials. The base beads were unreliable and insufficient for subsequent layer deposition. The rectangles show instances where the deposition deviated from the path which negatively affected deposition of subsequent layers. The circles indicate the uneven spread of molten material that directly affect the height of the bead at the corresponding locations. .... 49

Figure 28: The continuously printed specimen. Arrows indicate the printing direction. a) Front view. b) Oblique view from the front. c) Back view of the sample. d) Oblique view from the back. The wavy top layer was a result of uneven spread of the material and change in the heat input. The cavity was caused due to the deviation of the deposit from the planned path. .... 51

Figure 29: The CHF specimen. Arrows indicate the printing direction. a) Front view. b) Oblique view from the front. c) Back view of the same sample. d) Oblique view from the back of the same sample. .... 51

Figure 30: SEM micrographs of specimens at the boundary of layers 5 and 6 where there is a uniform distribution of the microstructural features. (a) The conventionally printed specimen. (b) The CHF specimen. The dashed red lines indicate the boundary between the layers. .... 55

Figure 31: EDX analysis of a dark particulate at the boundary of the 6th and 7th layer of the conventionally printed specimen. Figure was obtained by randomly zooming into the boundary area. .... 55

Figure 32: SEM micrographs and EDX results of the large Tungsten particles in the (a) 1st layer, and (b) 7th layer of the conventionally printed specimen. The insert windows indicate the area for the EDX analysis. .... 56

Figure 33: The SEM micrograph of the unmelted/unmixed wire sheath in the 5th layer of the CHF specimen. The pink lines represent the detection areas for EDX analysis in which the data have been recorded in Table 4. .... 57

Figure 34: Layer-by-layer hardness value for both specimens. Each data point is a numerical average of 7 data points on each layer and the error bars indicate the range of the collected measurements. ....	59
Figure 35: Layer-by-layer composition of Co, Fe, and Cr for both samples extracted from EDX analysis of the specimens. The drop in the composition of Fe from first to second layer indicates that the effects of substrate-dilution disappear. ....	60
Figure 36: Experimental setup for PAW-AM at Carleton University .....	64
Figure 37: Illustration of the weld pools created based on a) GTAW, b) PAW.....	65
Figure 38: Final configuration of the wire and the torch for PAW-AM experiments. ....	66
Figure 39: 3 beads with identical printing parameters (Current=25 A, Travel Speed = 100 mm/min, Wire Feed rate = 210 mm/min). The effect of wire and arc alignment can be visualized from top to bottom. ....	69
Figure 40: The beads printed with the conventional printing method of similar printing parameters (10 mm of arc length, Current=28 A, Travel Speed = 90 mm/min, Wire Feed rate = 270 mm/min) .....	70
Figure 41: a) Oxidation samples as described in Section 5.2.3. (b) An example of the shades of grey on Sample 1 along with the EDX results. ....	71
Figure 42: Images of the two printed samples at front and back view. ....	73
Figure 43: Overall cross-sectional SEM macrograph of the samples A and B. Yellow arrows indicate unmelted wire, and blue arrows indicate lack of bonding between layers. (Please note that lens distortion effect has caused the substrate arc).....	74
Figure 44: SEM micrograph of a fully melted section towards the center of the 5th layer in a) Sample A and, b) Sample B.....	75



## **Preface**

This thesis includes a peer-reviewed journal article:

S. Shahryari Fard, H. Frei, X. Huang, and M. Yao, “Coordinated Heat and Feed Printing Strategy for Wire and Arc Additive Manufacturing of Metal-Cored Wires,” *Journal of Materials Engineering and Performance*, 2021.

This paper has been integrated into this thesis with its entirety, however, the figure/table numbers, section numbers, formatting, and the reference have been adjusted according to the thesis.

The author of this thesis, Shahryar Shahryari Fard, was responsible for the equipment setup, design of the experiments, performing the experiments, data analysis, writing, and editing of the paper.

---

Shahryar Shahryari Fard

---

Dr. Hanspeter Frei

---

Dr. Xiao Huang

## Acronyms

AM	Additive Manufacturing
CMT	Cold Metal Transfer
CNC	Computerized Numerical Control
CHF	Coordinated Heat and Feed
DED	Directed Energy Deposition
EBM	Electron Beam Melting
EDX	Energy-Dispersive X-ray Spectroscopy
GMAW	Gas Metal Arc Welding
GTAW	Gas Tungsten Arc Welding
HAZ	Heat Affected Zone
HWAAM	Hot-Wire Arc Additive Manufacturing
LENS	Laser Engineered Net Shaping
Metal-AM	Metal Additive Manufacturing
PAW	Plasma Arc Welding
SLM	Selective Laser Melting
SLS	Selective Laser Sintering
SM	Subtractive Manufacturing
TMC	Titanium Mesh Cage
WAAM	Wire and Arc Additive Manufacturing

## **Chapter 1: Introduction**

### **1.1 Motivation**

Metal Additive Manufacturing has the potential to disrupt the broader engineering industry by empowering designers and manufacturing engineers with an added flexibility and complexity for their designs. Designing additively manufactured products faces less constraints compared to products that are designed for other manufacturing techniques, this allows production of some components that were previously impossible to manufacture. Subsequently, additive manufacturing streamlines the manufacturing process selection which can contribute to lowering the production cost. Furthermore, some low-cost additive manufacturing techniques (such as Gas Tungsten Arc Welding and Plasma Arc Welding) substantially reduce the material waste in addition to enabling the utilization of hard-to-machine materials. The material waste from wire-based metal additive manufacturing techniques is in fact one of the lowest, however, some materials are difficult to form into wires and are only available in powder form. Metal-cored wires can be manufactured by rolling the thin-metallic sheath into tubes while filling them with any compatible powder. However, additive manufacturing processes need to be adapted for these metal-cored wires.

### **1.2 Objective**

The overall goal of this work is to investigate the prospect of wire additive manufacturing with Stellite 6 metal-cored wire using Gas Tungsten Arc Welding (GTAW) and Plasma Arc Welding (PAW). The thesis was divided in to following specific objectives:

- Retrofitting a low-cost, custom-made, Computerized Numerical Control (CNC) printer with GTAW and PAW power supplies.
- Performing preliminary WAAM experiments with the Stellite 6 metal-cored wire using GTAW and PAW in order to achieve steady uniform straight beads.
- Printing and metallurgical analysis of multi-layer walls with Stellite 6 alloy to find the favorable printing strategy and corresponding parameters.

### **1.3 Thesis Overview**

This thesis includes an integrated peer-reviewed article on the work done with GTAW method. For consistency and cohesion, the thesis was divided into the following chapters:

**Chapter 1: Introduction** – This current chapter includes the motivation, objectives and overview of the thesis.

**Chapter 2: Literature Review** – This chapter is a review of metal additive manufacturing and the associated background information required for the following chapters.

**Chapter 3: Printer Modification and PAW Adoption** – This chapter outlines the improvements made to the CNC printer to enhance print quality and repeatability. Also, the work to retrofit the printer with a PAW power supply is described.

**Chapter 4: Coordinated Heat and Feed Printing Strategy for Wire and Arc Additive Manufacturing of Metal-Cored Wires** – This chapter is comprised of the peer-reviewed journal article which describes printing thin walls using the GTAW method. It elaborates on the preliminary printing results as well as a discussion on the final printed components.

**Chapter 5: Investigation on WAAM of Stellite 6 Metal-cored Wire with PAW** – This chapter elaborates on the preliminary experiments and associated results collected by PAW system.

**Chapter 6: Conclusion and Future Work** – This chapter summarizes the work performed towards the objectives and recommends further research directions to modify the wire and arc additive manufacturing of metal cored wires for thin-wall components.

## **Chapter 2: Literature Review**

### **2.1 Metal Additive Manufacturing**

Metal Additive Manufacturing (Metal-AM) is a subcategory of Additive Manufacturing (AM) defined by the ASTM as a process of joining material to build a component [1]. In AM, contrary to the more established Subtractive Manufacturing (SM) processes such as machining and chemical milling, a component is usually built by depositing the material layer by layer. Despite the complexity, the AM process allows for manufacturing a wider range of shapes and integrated structures resulting in extensive elimination of assembly and improves manufacturability [2]. Metal-AM has gained increasing attention across the world due to its revolutionary nature. For instance, the first of multiple Manufacturing Innovation Institutes, announced by President Obama in 2012 in order to further develop manufacturing technologies, was established for AM [3], [4]. In 2014, the government of Quebec initiated a network of experts to support the development and utilization of additive manufacturing amongst the businesses in Quebec [5]. Lastly, in July 2021, the Federal Economic Development Agency for Southern Ontario (FedDev Ontario) granted \$8.2 million to University of Waterloo for helping local companies adopt the technology [6]. Previous examples indicate that the governments are racing to revamp manufacturing industry in their respective regions to benefit various local industries. Some industry transformations by Metal-AM are reviewed here.

#### **2.1.1 Metal-AM in Aerospace**

Blakey-Milner et al. [7] suggested that Metal-AM improves both the financial and performance aspects of the Aerospace industry by means of:

- Reducing the cost and lead-time.
- Utilizing unique materials.
- Reducing component mass by allowing flexible design and increased design efficiency.
- Compacting multiple components into a single piece for better performance and risk reduction.

These effects can be discussed by looking into multiple examples.

At the RAUG Holding, an Aerospace company, the antenna brackets for Sentinel Satellites were topologically optimized and additively manufactured resulting in 40% in weight reduction and 30% more rigidity [8]. Figure 1 shows the development of the antenna through topology optimization of the initial design. The topology optimization seeks to optimize the placement of the material (structural elements) based on the defined physical and performance criteria, and AM is deemed ideal for producing the topologically optimized components due to its freedom [7], [9]. The original bracket design included multiple pieces which translates into assembly and its related cost. In addition to additively manufacture the optimized bracket out of AlSi10Mg, the company certified the component for use in outer space.

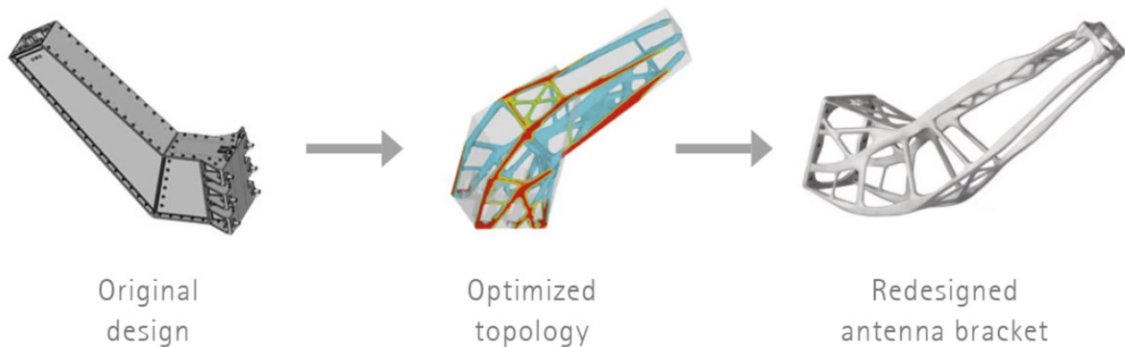


**Figure 1: Antenna bracket redesign process [8]**

Furthermore, Metal-AM has enabled cost reduction due to compaction of several pieces into one. Additive manufacturing technologies were utilized for more than one third of the GE9X turboprop engine components (Figure 2) [10]. The enlarged portion of the heat exchanger on the top right corner of the figure was additively manufactured into a single component. Traditionally, it was made from 163 components, and was 40% heavier, and 25% more expensive.

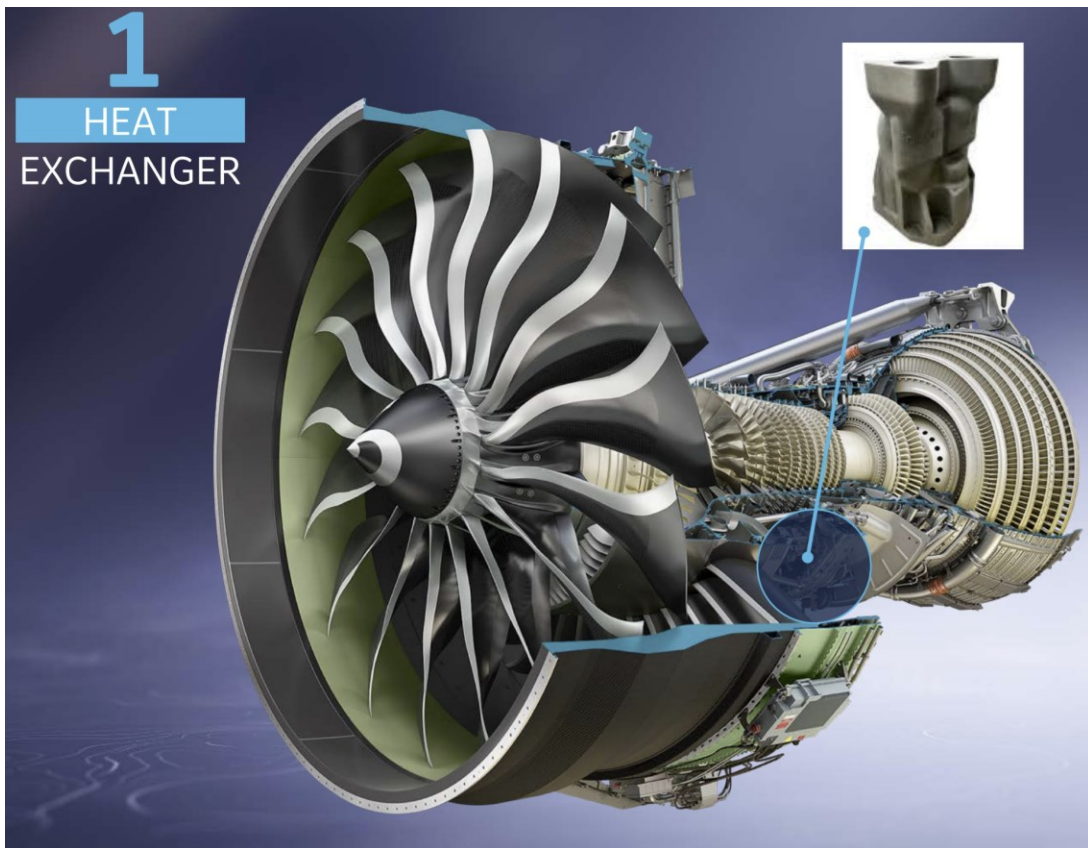


**Figure 2: GE9X turboprop engine and the heat exchanger that was additively manufactured resulting in lower weight, cost, and number of components [10].**

### **2.1.2 Metal-AM in Biomedical Industry**

Biomedical industry, specially the orthopaedics, has focused on adoption of Metal-AM due to the following needs [11]–[13]:

- Manufacturing patient-specific implants at the health care centers.
- Lower cost of customization as no molds and complicated tooling are required.
- Ability to integrate pores into the implants in order to simulate a natural bone structure for improving tissue in-growth.

In a medical procedure, to correct Cervical Spondylotic Myelopathy (CSM) (compression of the spinal cord is resulted due to the degeneration of spinal components [14]), one option is to implant a Titanium Mesh Cage (TMC) filled with morselized bone to decompress the spinal cord and restore the original height of the disc space and allow for bony fusion of the adjacent vertebrae [15]. One possible complication of this surgical procedure is the subsidence of the TMC into the adjacent vertebrae which can result in recurring spinal cord compression and delayed bony fusion [16] [17]. A possible reason for subsidence is the presence of sharp corners during the manual trimming of the TMC based on the anatomy of the affected area. As shown on Figure 3, Lu et al. [17] utilized Metal-AM to manufacture TMCs based on the patient anatomy which in this instance lowered the TMC subsidence.

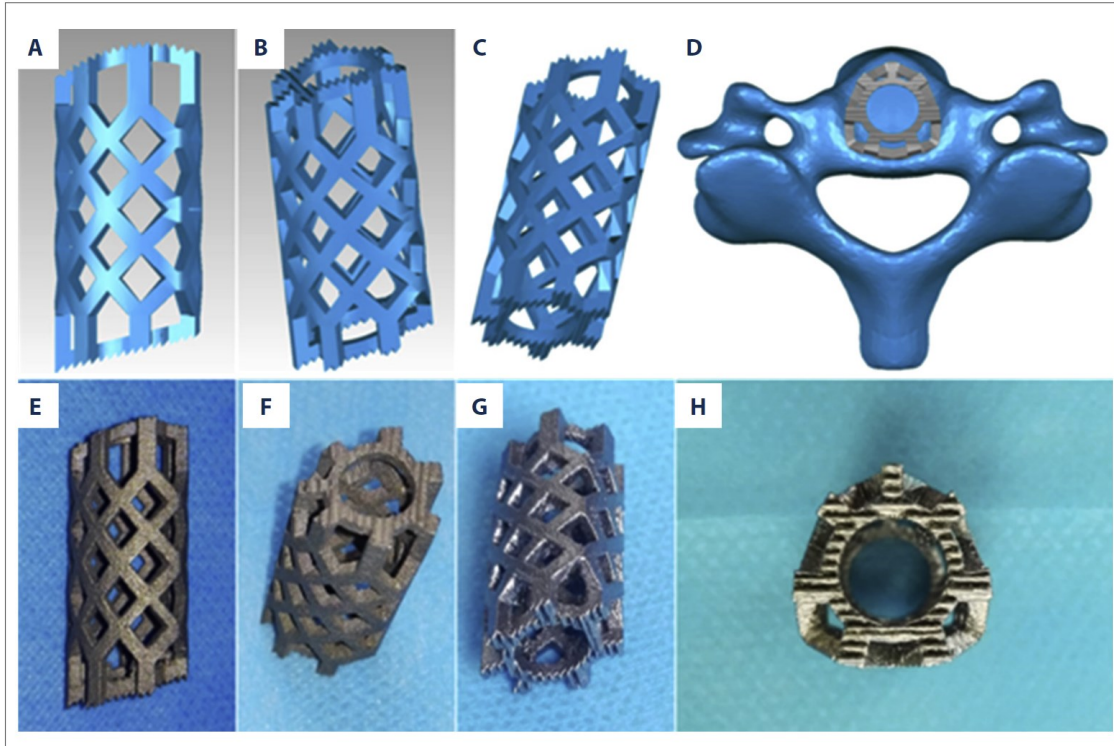


**Figure 3: The Anatomy-Adaptive Titanium Mesh Cage designed for subsidence prevention. A-D, CAD model of the TMC. A-H, additively manufactured TMC [17]**

Even though Metal-AM provides manufacturing and design freedom, this is a relatively recent technology and it did not found a broad adaptation, mainly due to the complexity of the process. Next, a brief discussion on economics of AM is provided.

## 2.2 Economics of Metal-AM

There are multiple factors affecting the cost of Metal-AM [18]–[21]. The study of the economics provides an overview of constraints and opportunities in Metal-AM. The production cost is estimated from the following equation [20]:

$$\text{Cost} = \text{Machine Purchase Cost} + \text{Operation Cost} + \text{Materials Cost} + \text{Labor Cost}$$

The calculation of the *Machine Purchase Cost* is based on the print time, and the entire time that the machine is expected to operate during its life. The *Operation Cost* is related to the

portion of the overhead costs such as maintenance, utility, etc. that was spent during the print time with respect to the overall life of the machine. Furthermore, the *Materials Cost* covers the cost of the feed stock that is used for printing. The material usage is dependent on the process and the type of the feed stock that will be discussed later, however, the weight of the component, the weight of the support structure, and the unrecyclable wasted feed stock in some processes constitute the *Materials Cost*. Finally, the *Labor Cost* refers to the cost of the workforce necessary for performing the manufacturing; however, the time that a laborer spends is different from the build time [20], [22].

Ding et al. [21] recently expanded on AM cost modeling and discussed the hidden cost of process failure where the component is either unfinished or defective. They adopted Mean Time Between Failure approach from reliability engineering in order to model the cost of failure which is assumed to be unsystematic. According to their process map represented in Figure 4, a failure can occur any time before the product inspection.

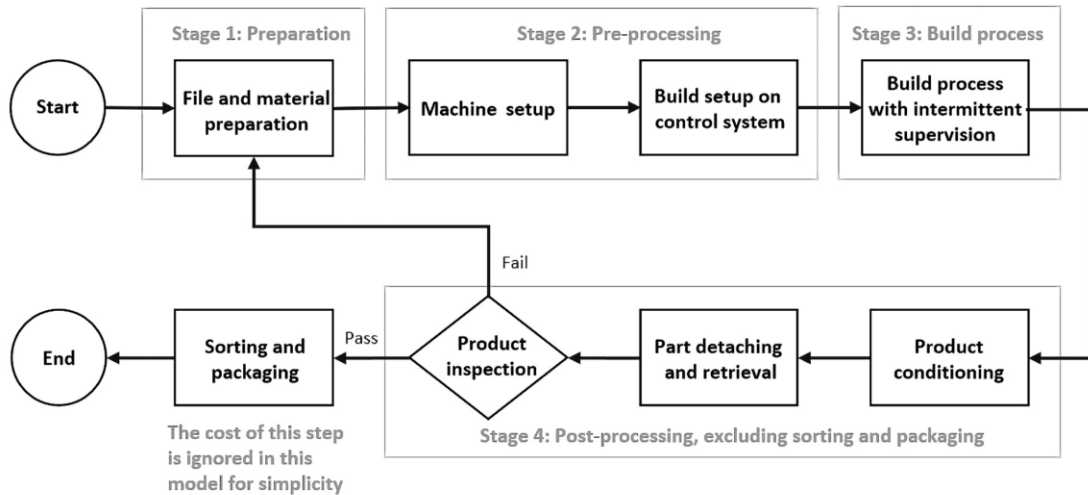


**Figure 4: AM process map represented by Ding et al. [21] for the material jetting process. The steps provided in this map are common among the other AM processes.**

Additionally, Figure 4 provides a clear perspective on the materials, operations, and labor costs discussed earlier. As mentioned, the type of process affects the economics, and the performance of AM. Aerospace and biomedical industries benefit from Metal-AM due to customizability and high performance features. Next, the types of Metal-AM based on the feed stock is discussed.

### **2.3 Types of Metal-AM: The Feed Stock Perspective**

Metal-AM is a growing industry and evolves rapidly. Current metal-AM prints can be categorized into:

Powder Bed Systems

Powder Feed Systems

Wire Feed Systems

The last two processes can be combined into Directed Energy Deposition (DED) technologies [23]. Direct injection of the material into the molten pool is the distinguishing characteristic of DED.

#### **2.3.1 Powder Bed Systems**

Powder bed systems utilize usually a laser as power source to melt a thin layer of powder that is laid on top of a previously melted layer in order to create a component [1]. The main process associated with powder bed systems is Selective Laser Melting.

##### **2.3.1.1 Selective Laser Melting (SLM) Selective Laser Sintering (SLS)**

Figure 5 represents the schematic of a SLM system which uses a laser that is scanned over the powder bed to melt powder according to the required parts geometry. In this particular example, the motion of the beam is controlled by the F- $\theta$  lens whereas the beam focus is

controlled by a galvanometer [24], [25]. The SLM systems are often programmed to fuse the edges of a component before fusing the infill powder [24]. Laser power and scanning speed are the main parameters that affect the material properties and any defects in the part's microstructure [26]. SLS is a similar method where the material is partially melted as the layers are deposited [27], [28].

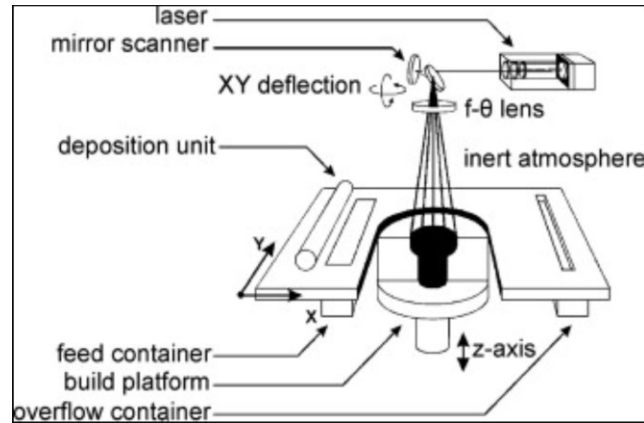


**Figure 5: Diagram of a SLM powder bed system [25]. The laser is the power source for melting the 20-100um powder layer to build a component.**

The extensive research on the SLM systems has led to multiple mass-produced systems. Röttger et al. [29] compared 4 different machines producing identical Stainless Steel 316L samples based on their respective recommended parameters. Even though the microstructure of the samples were found to be similar to each other, the density of defects in the samples were different.

### **2.3.1.2 Electron Beam Melting (EBM)**

The EBM process shares similar characteristics with the SLM method, however, EBM utilizes an electron beam, therefore, it requires a vacuum for operation [24]. The vacuum

prevents contamination of the melted powder and heated deposit while the electron beam ensures total melting of the powder for creating denser components. The lack of contaminations and solidity of the layers distinguish the EBM process as the preferred process for producing orthopaedic implants [24], [30]. The printing for the EBM process can be performed at elevated temperatures which prevents distortion and warpage [24].

In both SLM and EBM, the powder can be reused assuming a proper sieving process is undertaken, however, it is important to note that the characteristics (such as shape, particle size distribution and surface morphology) of the powder may change, and the engineers must ensure the powder does not reach a point where the process parameters require modification [31]. SLM and EBM are the two main powder-bed processes, the powder-feed system types will be discussed next.

### **2.3.2 Powder Feed Systems**

Powder feed blows the powder into the weld pool of the preceding layer using a nozzle that is aligned concentrically around the heat source [1]. In addition to manufacturing large-scale components, powder feed systems can be used for repair. The most common process in this category is Laser Engineered Net Shaping which will be discussed next.

#### **2.3.2.1 Laser Engineered Net Shaping (LENS)**

One of the earliest documents on this process indicates its development at Sandia National Laboratories in the United States in 1998 [32]. As shown on Figure 6, this process includes many parameters that need to be controlled [33]. Travel speed, laser power, laser focal

point diameter, and powder feed rate are some of the operating parameters that depend on the powder properties [33]. In general, larger and more spherical powders are required as the larger diameter of the powder prevents porosity as less of the environmental gases are entrapped amongst the powder particles.

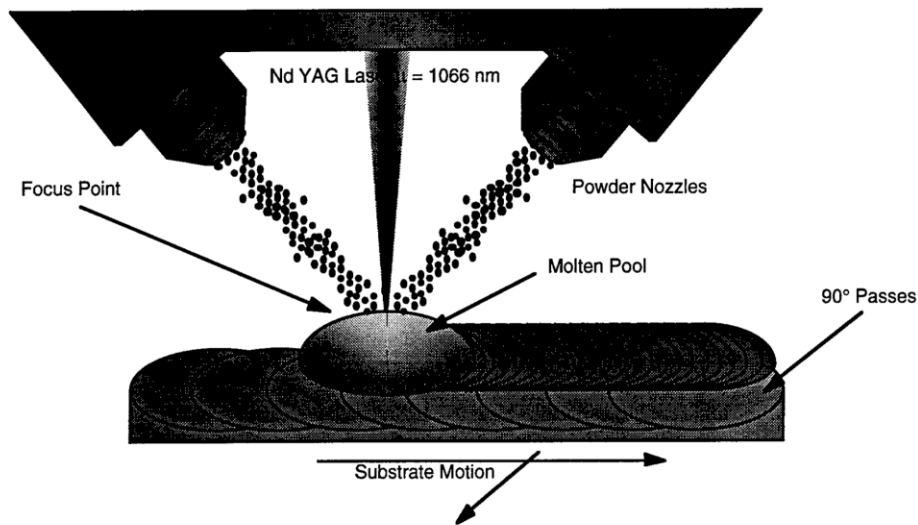


Figure 6: A system depicting the LENS process for Powder Feed Metal-AM system [32]. The powder is blown onto the area that is melted by the laser.

### 2.3.3 Wire Feed Systems

Metal-AM with wire uses electron beams, lasers, or electric arc to melt the wire as it is fed over a path [1]. Electric arc-based processes are the least complex, allow more varieties of materials, and have higher building rates compared with other heat sources [34]. Additionally, the component size is largely dependent on the printer which is usually low-cost in the case of wire feed systems [35]. The challenges in Wire and Arc Additive Manufacturing (WAAM) are lower dimensional accuracy and surface finish compared to powder feed systems [36]. Due the relative high-power input, the part accuracy is affected by distortion and shrinkage during the various heating and cooling phases of

manufacturing, and any geometric defect is multiplied as subsequent layers are deposited [36]. Furthermore, the real-time quality verification/mitigation in WAAM processes is difficult as the common Metal-AM defects such as porosity, oxidation, and crack formation occur due to environmental factors (oxidation for example), process instability, and inadequate parameter selection. The main types of arc based WAAM systems will be discussed next.

### 2.3.3.1 Gas Metal Arc Welding Additive Manufacturing (GMAW-AM)

As shown on Figure 7, Gas Metal Arc Welding (GMAW) system initiates an arc between the wire and the substrate causing them both to melt [37] The wire, with + potential, is constantly fed onto the Weld Bead, with - potential, by the wire feeder, and it is melted by its internal resistance. Bead geometry is significantly affected by the relative motion of the torch and the plate.

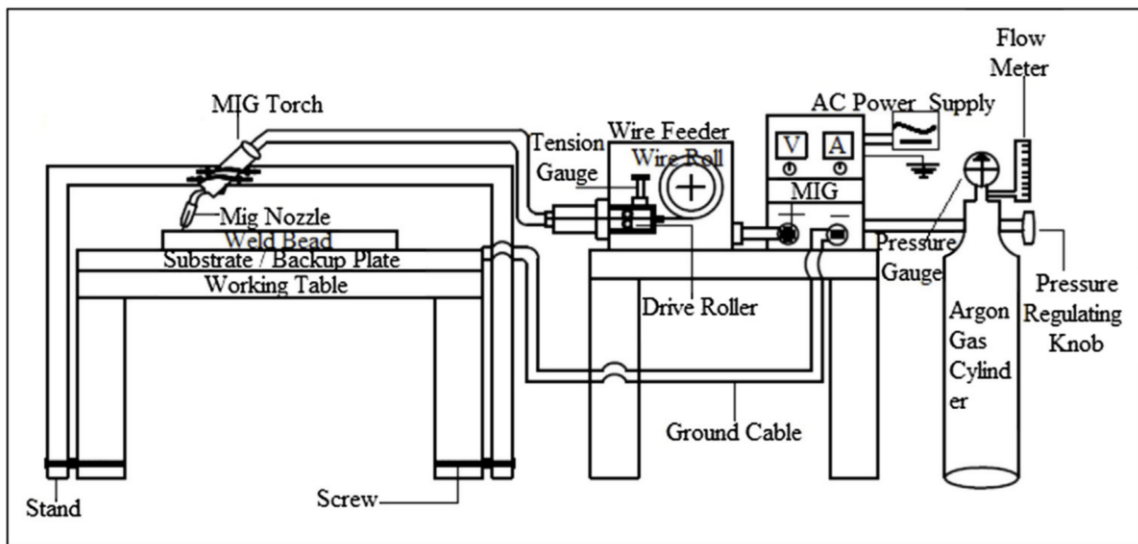
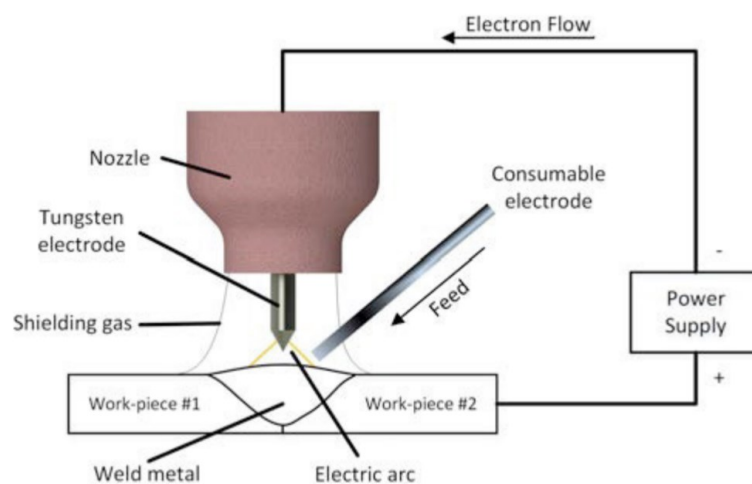


Figure 7: Schematic of the Gas Metal Arc Welding Additive Manufacturing setup [37]

One of the most well-known GMAW based AM processes is the Cold Metal Transfer (CMT) method. This process utilizes a reciprocating wire in order to create molten droplets as the current is pulsed [38]. The reciprocating scheme of the wire is adjusted based on the arc length measured automatically. This process improves the arc stability and helps to have a less wavy surface [39].

### 2.3.3.2 Gas Tungsten Arc Welding Additive Manufacturing (GTAW-AM)

In GTAW-AM, the substrate is connected to a base and the torch can travel over it; however, the wire is fed separate from the nozzle. The schematic of the heat source is provided in Figure 8 where the arc exists between the Tungsten electrode and the substrate [40]. The welding current, wire feed rate, torch travel speed, and the shielding gas flow rate are the main parameters that can be adjusted under this configuration. The increase in the welding current and the wire feed rate increases the thickness of the walls [41]. The melt through depth of the beads increase as the travel speed increases [42].



**Figure 8: Schematic of GTAW system which is shown to weld two pieces by adding the filler metal [40]. The consumable electrode can be a wire.**

Compared to GMAW, GTAW is suitable to deposit wider selection of materials and have little to no spatter; however, this welding method is more complex, and supports limited welding positions (such as up-side-down welding). The heat input density of a 3.2 mm dia. Tungsten electrode was measured by Aibe et al. [43] at 3 different current setpoints (shown on Figure 9) which shows the highest heat input at the center of electrode.

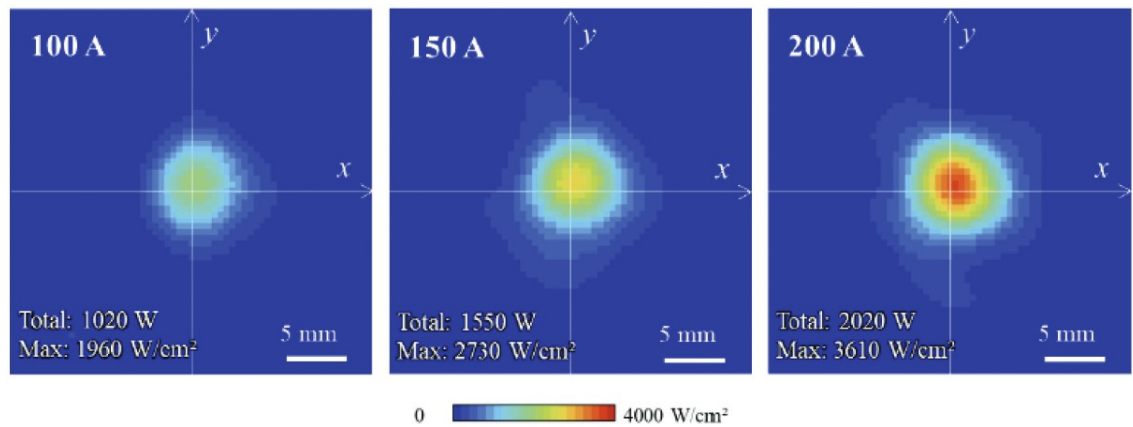


**Figure 9: Heat input density of a vertical GTAW system measured by Nestor's water-cooled split anode copper plate [43].**

### **2.3.3.3 Plasma Arc Welding Additive Manufacturing (PAW-AM)**

This type of Wire and Arc Additive Manufacturing (WAAM) is similar to GTAW-AM where the wire is melted by the arc as the heat source moves over the substrate. However, the Plasma Arc Welding (PAW) torch (Figure 10) is more complex than GTAW torch. In PAW, a pilot arc is first established between the electrode and the plasma nozzle for enabling the ignition of the main arc between the electrode and the substrate [44], [45]. The non-transferred arc is formed between the electrode and the plasma nozzle, whereas the transferred arc is formed between the electrode and the workpiece [46]. The hot Plasma Gas passes through the orifice of the nozzle to gain speed. Despite high capital and operation cost, PAW is more energy efficient, provides more penetration, and protects the

electrode for a longer use, as compared to GTAW [44]. The associated parameters in PAW, such as welding current and speed, affect the weld bead similar to that of GTAW [44]. The increase in the welding current widens the bead, whereas faster travel speed creates narrower bead.

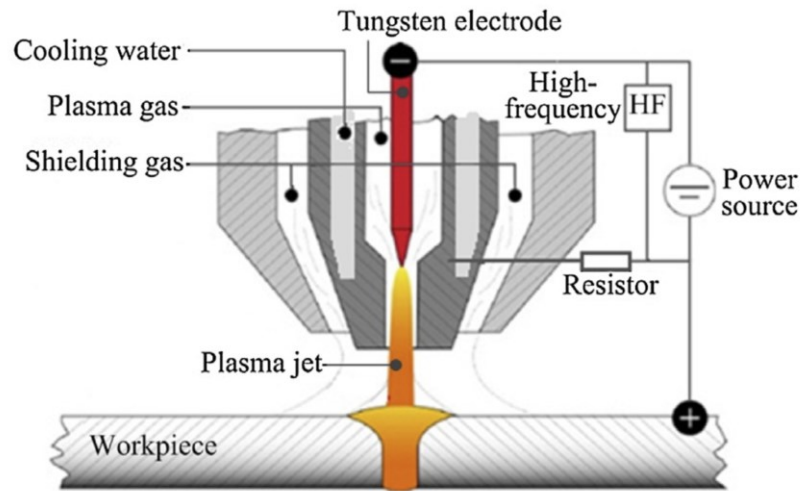


**Figure 10: Schematic of PAW torch where the dark gray component is the plasma nozzle (not labeled by the reference) [45].**

After reviewing different Metal-AM processes, it is important to briefly discuss the materials and microstructure in arc Metal-AM.

## 2.4 Materials and Microstructure in Metal-AM

Ti, Al, Stainless Steel, and Superalloys are the main materials that have been commercially used [1]. Accumulation of residual stress during the manufacturing and failing to relieve it causes cracking and plastic deformation in the material [47], [48]. Furthermore, the porosity caused by contamination in the material, or disruption in the deposition process

causes low mechanical strength and poor fatigue performance [44]. Therefore, materials research is necessary for producing a component.

In addition to the operational parameters, the thermal history of the layers (the quantity and amounts of heating as more layers are deposited) affects the microstructural properties and hence the mechanical properties of the printed component [49]. For instance, Sahoo et al. [50] discovered that the pores increase in number and volume along the building direction of a vertical Ti-6Al-4V cuboid.

#### **2.4.1 Superalloys**

Superalloys have been developed for applications where the operating temperature is extremely high and severe fatigue and creep conditions may be present. Fe, Co, and Ni are the elements which form the basis of the superalloys. The development of superalloys began in the aerospace industry as gas turbines needed to run at a higher temperature to increase efficiency. The gas turbines mainly used Ni-based superalloys, however, Co-based alloys, such as Stellite 6, were developed for applications that required higher strength [51].

#### **2.4.2 Stellite 6: A Co-based Superalloy**

Stellite 6 is one of the most well-known superalloys that was developed for applications that wear and corrosion are present at high temperatures such as coating on gas turbines in the aerospace industry [52]. In addition to Co as the major constituent, Cr, Ni, and W, exist in the composition of Stellite 6. The Cr carbides are responsible for hardening the material while Cr oxides improve the corrosion resistance. The mechanical strength of Stellite 6 is also improved due the presence of W in an intermetallic phase. Figure 11 illustrates the microstructure of a cast Stellite 6 sample where the Eutectic region with a darker shade

represents the carbides [53]. On the other hand, the Co-rich  $\gamma$  solid solution is represented in the lighter regions.

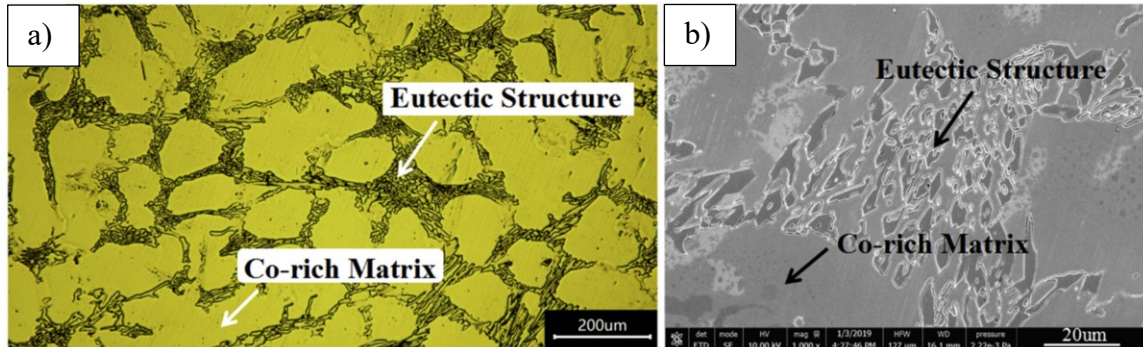


**Figure 11: a) Optical micrograph of cast Stellite 6 superalloy. b) SEM micrograph of cast Stellite 6. Both micrographs include the labels regarding the microstructure [53].**

## 2.5 Advantages and Disadvantages of Metal-AM

Although the benefits and limitations of Metal-AM have been mentioned throughout the thesis, a summary is provided herein.

The potential advantages of Metal-AM can be summarized as follows:

- Production of high value customizable parts in small batches is made possible since AM does not require die, mould, or jig manufacturing [54]–[56]. Replicating a product by means of reverse engineering benefits from 3D scanning and AM. CT-scans were reported to be used for additively manufacturing implants by scanning the respective bone [48], [57].
- Complex geometries can be additively manufactured which help to reduce the number of components while helping to integrate more functions into the products [48], [58],[59].

- Metal-AM can be utilized to print costly materials such as Titanium since material waste is reduced [60], [61]. Furthermore, additively manufactured parts have shown better mechanical properties due to finer microstructure [62]. As a result, Metal-AM contributes to improved performance and energy savings. For example, it has helped increasing the power-to-weight ratio of aerospace components [25].

The disadvantages of Metal-AM can be summarized as follows:

- Capital investment and lack of skilled engineers and technicians in the field [45], [57].
- Depending on the process, the lack of post-processing causes a lot of problems such as fatigue-prone surface finish, incomplete layer bonding, and poor dimensional resolution [63].
- Modeling of the Metal-AM processes and monitoring the processes present significant challenges [64], [65]. Till today, there is no in-situ process modification in place during the printing.
- Layer-by-layer deposition of material in some processes causes conflicting mechanical behaviors (such as anisotropic properties) among the consecutive layers that is rooted from the reheating of the previous layers [66].
- Metal-AM processes is extremely challenging. Material, part geometry, heat source and environmental factors such as humidity can affect metallurgy [67].

## Chapter 3: Printer Modification and PAW Adoption

Within the duration of this research, two welding systems were used (GTAW and PAW) together with Metal-Cored Stellite 6 Wire. A brief description of the wire and the 3D printing system is presented here.

### 3.1 The Wire: Ø1.2 mm Metal-Cored Stellite 6 Wire

Metal-cored wires consist of a rolled sheath and packed metallic powder within. Figure 12b and c indicate the cross-sections of the Stellite 6 wire. A patent from the manufacturer of the wire indicates that the sheath is mostly Co with some minor amount of Fe [68].

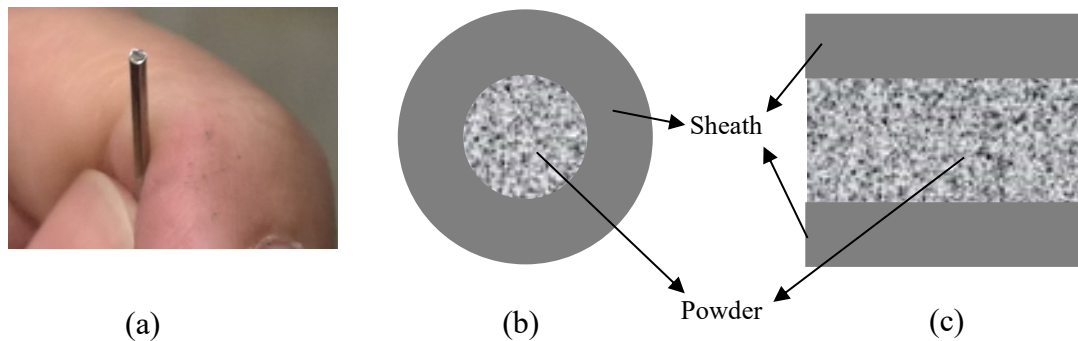


**Figure 12: Stellite 6 wire. (a) Image of the wire cross section. (b) Schematic of the perpendicular cross section of the wire. (c) Schematic of the lateral cross section of the wire.**

The specific composition and a description of the wire utilized for this study will be presented in Section 4.3. Generally:

- The wire is easily cut with a plier, but it may be deformed in this process.
- The wire is highly malleable and external forces can bend the wire.

- The seam fails when a compressive force is applied perpendicularly (relative to the wire's midplane passing through the seam) to the wire causing the powder particles to drop.

### **3.2 The Printer**

Figure 13 illustrates the custom Computerized Numerical Control (CNC) system that was utilized for this study. A metallic substrate is mounted on the print bed which moves along the Z-axis. The substrate is brought to appropriate arc length with respect to the welding torch and the wire nozzle that are attached to the horizontal manipulator plate. The motion and travel speeds are programmed through a set of codes known as G-code. Further control over the wire feeder and the welding equipment is also programmed through G-code.

This equipment has been previously utilized for creating multi-layer thin wall components using Hastelloy X [69]. This wire was 1.2 mm in diameter and fed continuously over previous layers and provided a uniform and repeatable bead. The microstructure, wear resistance, and oxidation behavior of the additively manufactured component were examined.

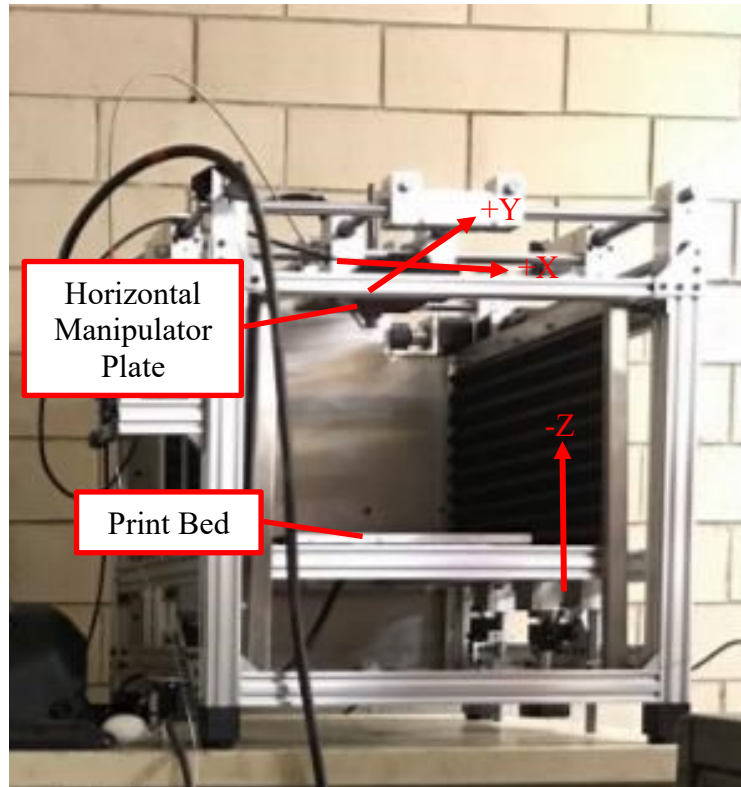


**Figure 13: The custom Computerized Numerical Control (CNC) machine for WAAM research at Carleton University.**

### **3.3 The Wire Feeding Mechanism**

Initially, a commercially available welding wire feeder was retrofitted with a NEMA 23 stepper motor to push the wire from a spool into the wire nozzle through a wire guide. The wire nozzle is located as close as possible to the arc to feed the wire into the weld pool. The wire guide needs to be flexible enough to allow the motion of the printer, but rigid enough to protect and guide the wire. Figure 14(a) shows the overall wire feeding setup, whereas Figure 14(b) represents the operation of the wire feeder where the wire is held against knurled driving rollers by means of hammering rollers that are controlled with the compression knobs.

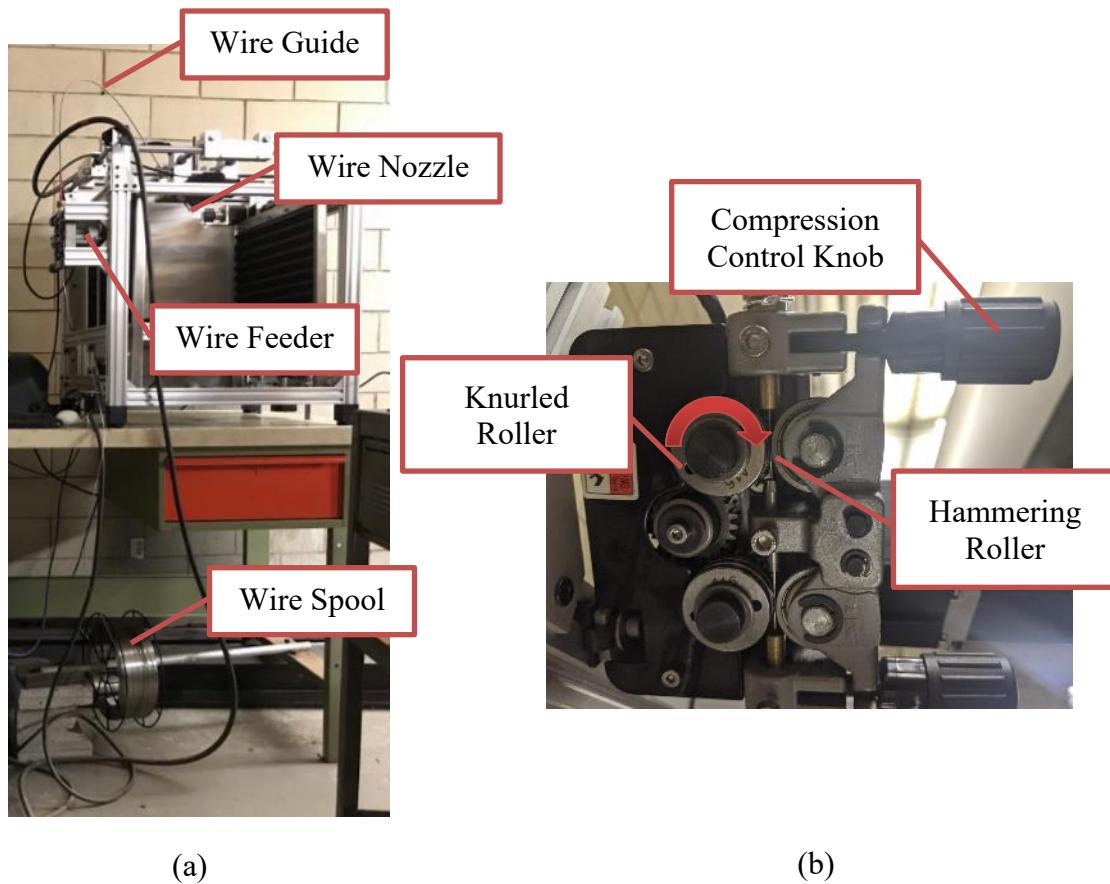


**Figure 14: The Original Wire Feeding Mechanism. (a) indicates the overall setup where the wire goes through the wire feeder and the wire nozzle. (b) The Wire Feeder close-up photo where the arrow indicates rotation.**

Furthermore, the wire nozzle system is at the last interface before the wire is melted, it is also the feature that controls the wire angle and helps to keep it straight. The wire nozzle support system is shown on Figure 15 where it is rigidly mounted to the power source and guides the wire through a brass wire nozzle.

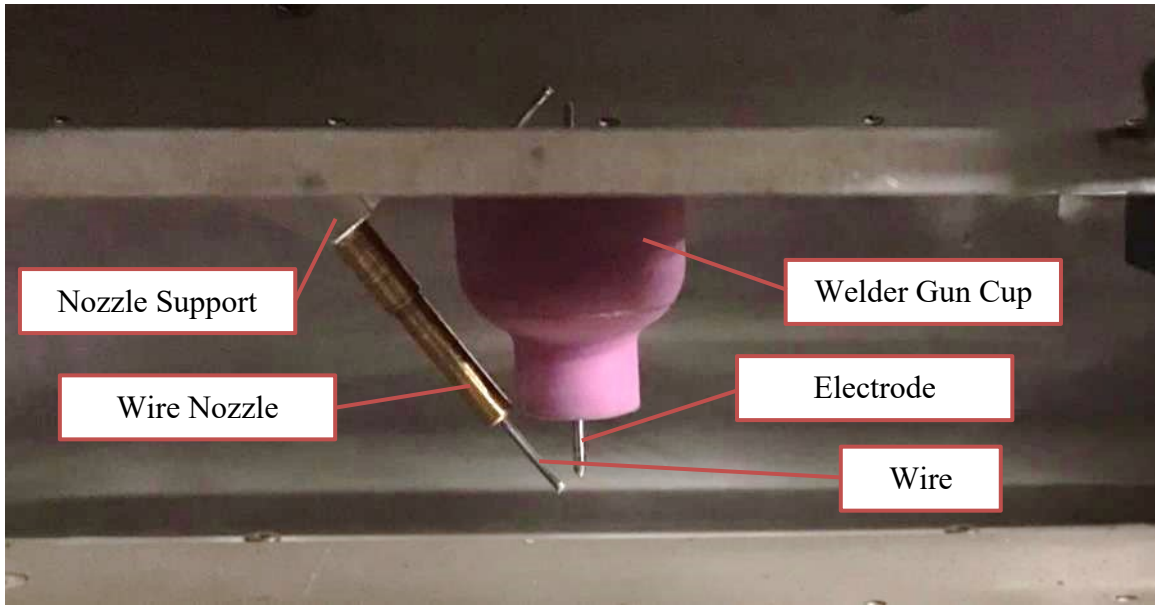


**Figure 15: Wire nozzle setup for the GTAW system. The setup is similar for the PAW system as well, the power source is perpendicular to the substrate and the wire is fed from an angle.**

Argon was selected as a shielding gas for both GTAW and PAW since it is more cost effective (comparing to He), safer (than H<sub>2</sub>), and has been previously used in related research [42], [70].

### **3.3.1 Shortcomings of the wire feeder**

The existing wire feeding system was not tailored for the flexibility of the metal-cored Stellite 6 wire. Here are some of the examples.

#### **3.3.1.1 Defective Wire**

Upon inspecting of the printed samples, some powder was discovered around the wire feeder rollers. It was also found that the applied force on the wire caused the seam to open, and the powder to fall off. The force was calibrated on both rollers to remedy the wire

compaction. This calibration method, as part of procedural modifications, requires the force to be adjusted until there is no wire slippage and then adding two rotations of the compression knobs. Effects of knurled rollers on the wire should be considered during the calibration by limiting the number of trials of new wires.

A second wire defect was discovered when the wire failed (or delayed) to exit the nozzle. Further investigation indicated that a kinked area in the wire hit the entrance of the nozzle as the cross-section was not circular anymore. Spool management (by means of rotation limitation and tensioning the wire) eliminated the issue although continuous inspection of the wire was performed.

### **3.3.1.2 Misalignment of the Wire and Power Source**

Based on the arc characteristics of GTAW and PAW, the optimal wire position during the process is at highest heat density below the arc center [43], [71]. Observations indicated that misaligned wire requires extra energy input to melt causing larger Heat-Affected Zone (HAZ) and uneven surface. As shown in Figure 16a, the deposited metal is not at the center of the HAZ which implies melting of the wire at a colder portion of the arc, hence excessive heating of the substrate. This effect becomes worse when the wire oscillates under the arc and melts at various rates along the bead. The main reason for the initiation of the oscillation could be the wire deflection caused by the weight of the molten droplet, and it is sustained by non-uniform melting rate and mass transfer as the wire begins to deflect from the center of the arc [72], [73]. Figure 16b illustrates this issue: the orange rectangle indicates the fully melted wire, the red circle shows the unmelted wire when it had been

furthest from the center of the arc, the yellow oval shows the wire oscillating under the arc while pushing the molten weld pool around, and finally, the blue circle indicates the wire melting away from the center of the arc.

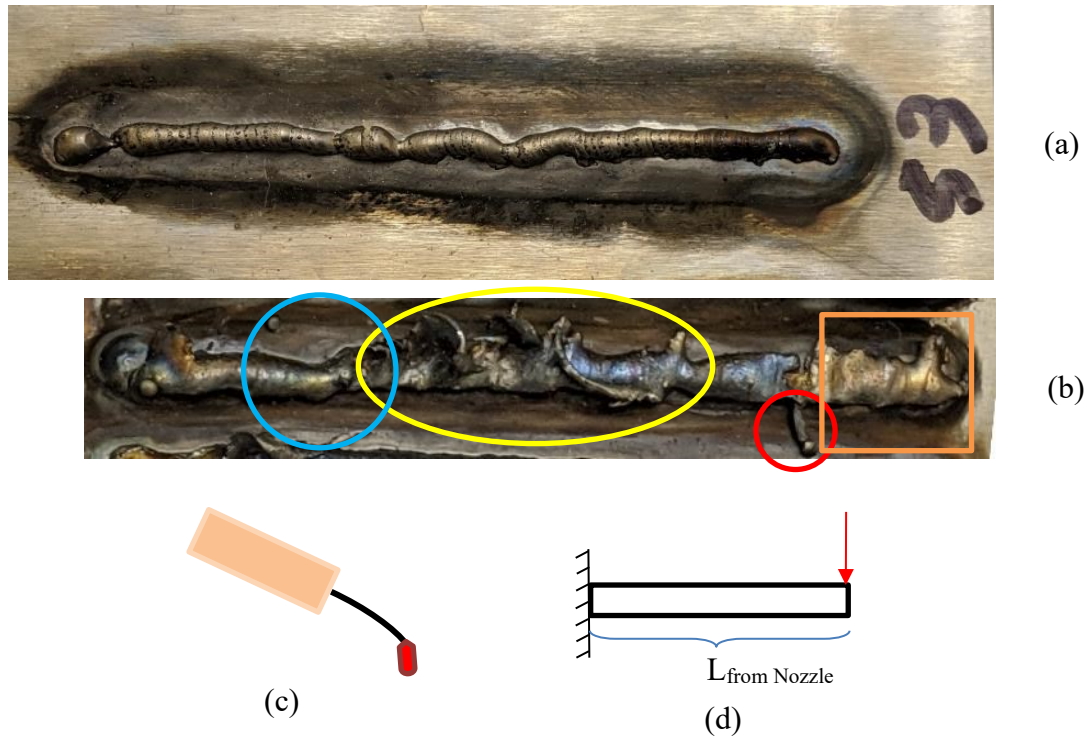


**Figure 16: Examples of Wire and Arc Misalignment.**

As shown in Figure 16c, the weight of the molten droplet inconsistently deflects the wire from the arc, it can be simplified by the free body diagram on Figure 16d. The deflection of the beam (at the tip) can be described based on the following equation [74]:

$$\delta = \frac{W L_{from\ Nozzle}^3}{3EI}$$

where, as shown on Figure 16d,  $W$  and  $L_{from\ Nozzle}$  are the force applied to the wire by the droplet and its distance from the nozzle outlet, respectively. Minimizing both

parameters reduces the deflection, however, the impact of  $L_{from\ Nozzle}$  is 3-fold.  $EI$  represents the flexural rigidity of the beam which is related to the geometry and material properties of the wire in the case of the wire nozzle and cannot be changed. Therefore, the only feasible adjustment for preventing oscillation of the wire under the arc is to minimize the distance from the nozzle outlet to the substrate where the weld pool is located.

### 3.3.1.3 Unwanted Wire Motion and Wire Slippage

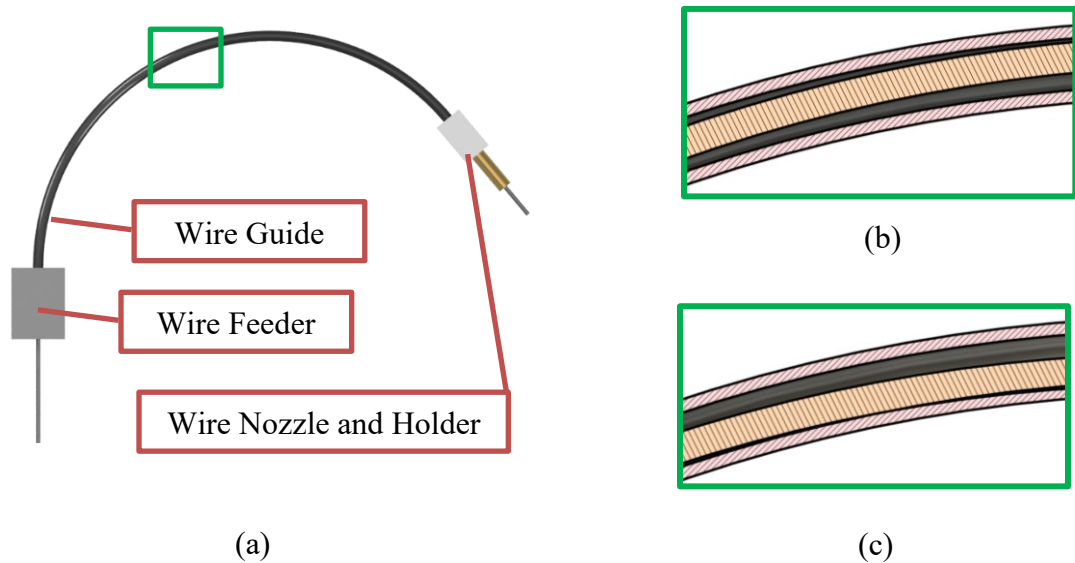
As shown in Figure 17, the expected starting locations varies despite similarly programmed start location and initiating wire length. Further investigation demonstrated that the slippage of the wire inside the wire guide is significant.



**Figure 17: An example of wire slippage. Bead 18 is shorter than Bead 19 even though the wire was cut similarly, and the beads were expected to begin at the same location, however, Bead 18 started about 1.5 mm after Bead 19 because of wire slippage inside the wire guide.**

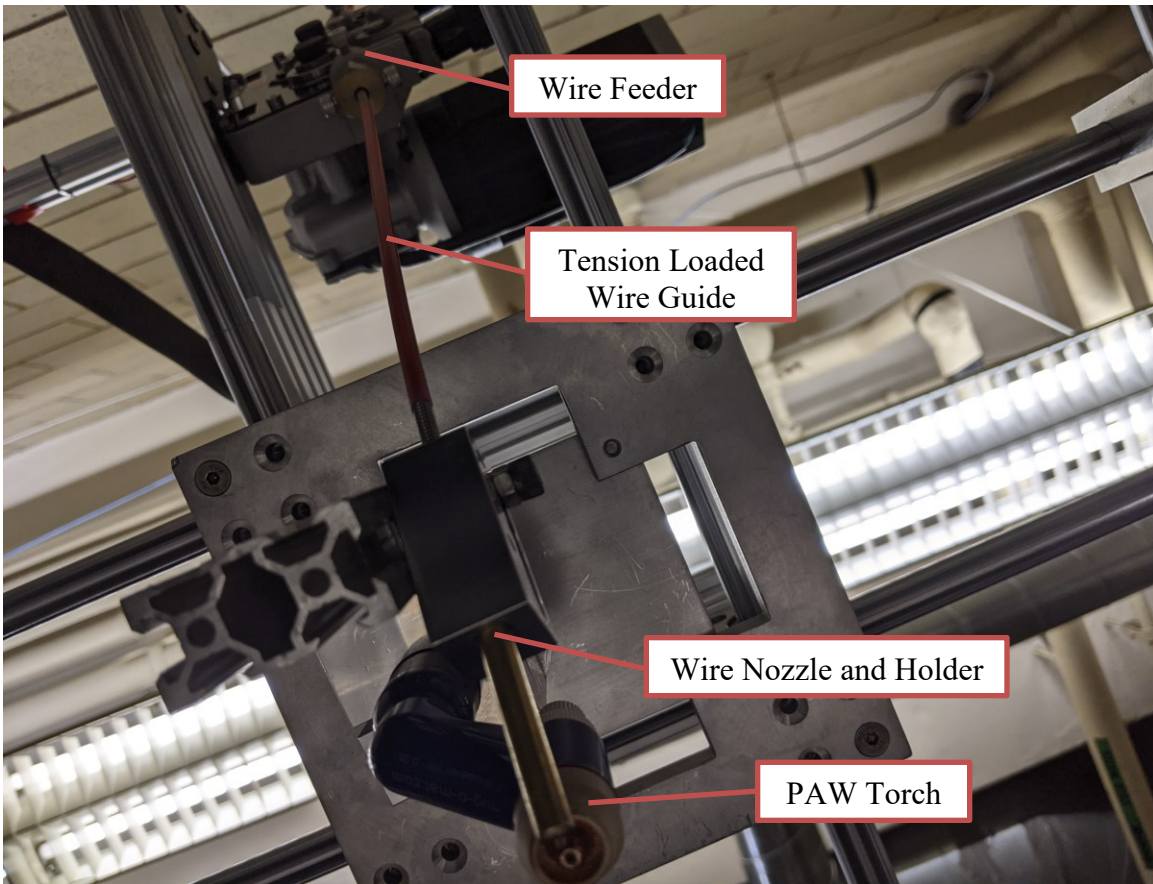
Figure 18 indicates the mechanism of the slippage where the wire feeder is fixed in place while the wire nozzle and holder are allowed to move relatively. As explained in Section 3.3, the wire guide must accommodate motion and protect the wire, and therefore, a spring guide was selected with a larger inner diameter than the wire to allow wire movement. In the example shown in Figure 17, the wire inside the wire guide had started its motion from the position in Figure 18c and the wire feeder had to compensate the length of wire needed

to reach Figure 18b position before the wire starts moving out of the nozzle where there is friction. Additionally, the spring effect of the wire guide could potentially absorb some of the wire displacement during the Wire Nozzle travel. A solution for the problem in Figure 17 can be eliminated by removing the clearance in the wire guiding system before printing.



**Figure 18: The slack in the wire guide. (a) wire feeding setup where the wire feeder and the wire nozzle and holder are fixed, however, they move relative to each other. (b) and (c) relative wire position (yellow hatch) and wire guide (pink hatch) when the wire is slightly pushed in and out of the nozzle, respectively.**

However, the main remediation strategy was to eliminate the flexibility of the Wire Guide, that is to directly feed wire from Wire Feeder to the Nozzle. Figure 19 indicates the bottom view of the modified Wire Feeder location where a fixed distance from the Wire Nozzle and Holder is maintained. The Wire Guide is tension loaded to protect the wire from buckling.

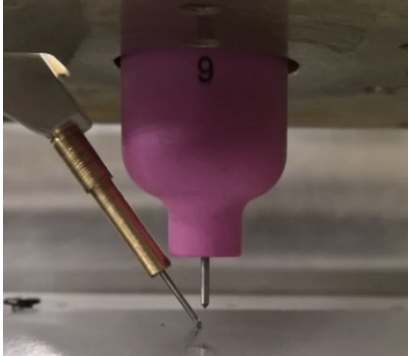


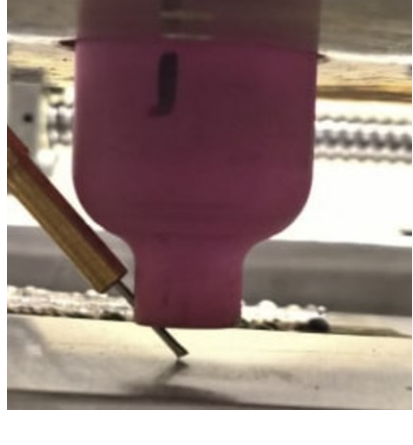
**Figure 19: The modified wire feeder location relative to the nozzle and holder. The wire guide (same spring) can be replaced with any rigid cylindrical tube to protect the wire. This setup can be utilized for both welding methods.**

### **3.4 Improvements to Gas Tungsten Arc Welding System**

The main improvement to the GTAW system was to reduce the distance between the Nozzle outlet and the welding pool as discussed in Section 3.3.1.2. The limiting factors for reducing the distance are the physical barriers to fit the nozzle and high temperature that could melt the nozzle. Table 1 represents several iterations of Torch-Wire configurations tested for this research along with the advantages and disadvantages.

**Table 1: Some of the torch-wire configurations tested to GTAW system**

Config. #	Photo	Advantage	Disadvantage
1		<ul style="list-style-type: none"> <li>- Large gas nozzle outlet can provide more shielding and prevent oxidation.</li> </ul>	<ul style="list-style-type: none"> <li>- The large cup prevents the Wire Nozzle to be in close proximity of the arc causing wire oscillation.</li> </ul>
2		<ul style="list-style-type: none"> <li>- The <math>L_{from\ Nozzle}</math> is reduced.</li> <li>- The cup is still large enough for preventing oxidation.</li> </ul>	<ul style="list-style-type: none"> <li>- The electrode is contaminated if there is any Wire-Arc misalignment.</li> </ul>
3		<ul style="list-style-type: none"> <li>- Larger cup prevents oxidation while having a shorter <math>L_{from\ Nozzle}</math>.</li> </ul>	<ul style="list-style-type: none"> <li>- Electrode contamination is less than Config. # 2.</li> <li>- A small wire-arc misalignment causes the wire to roll over the substrate and not melt.</li> </ul>

4		<ul style="list-style-type: none"> <li>- Electrode contamination of the wire is reduced as the cup prevents the wire from bending upwards.</li> </ul>	<ul style="list-style-type: none"> <li>- Acute nozzle-substrate angle increases the chance of Wire Nozzle collision with previous layers.</li> </ul>
5		<ul style="list-style-type: none"> <li>- Wire bending is constrained from the top, left, and right by the notch that was cut in the cup.</li> <li>- Wire oscillation is dampened by the notch and misalignment is reduced.</li> </ul>	<ul style="list-style-type: none"> <li>- The notch and the wire inside the cup disrupt the laminar Argon flow from the gas nozzle outlet which boosts oxidation.</li> </ul>

As described on Table 1, Configuration #5 addressed the main problems with the wire and arc alignment by implementing a notch in the cup as shown on Figure 20; the effects of this modification were significant, however, a small oscillation was present as the notch was not cut precisely. Furthermore, the electrode is set at the outlet of the cup, providing a better result (in terms of the stability of the arc) with an arc length of 3 mm and wire angle of 42° with respect to the vertical axis. Another operational hurdle occurred after a long printing experiment where cooling time was limited: excessive heat expands the notch and results in a loose fit that reduces the effectiveness of the notch.

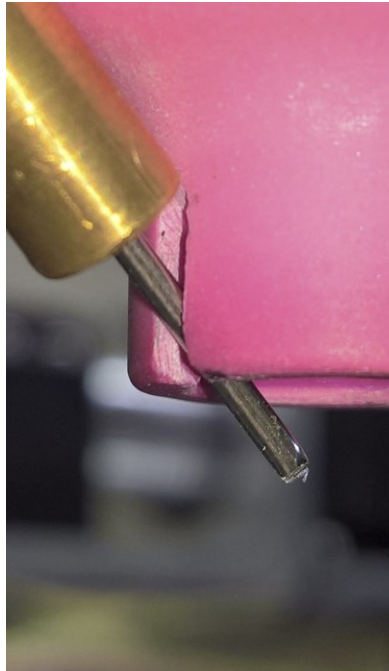


**Figure 20: The notch that was added to the cup to restrict the motion of the wire.**

Significant number of experiments were performed to improve the process in printing Stellite 6 metal-cored wire as has been summarized in Chapter 4.

### **3.5 The Control System Upgrade on the Printer**

As it will be discussed in Section 3.6, the adoption of the Plasma Arc Welding (PAW) system required an upgrade of the control board. Originally, the printer operated with a Smoothieboard [75] that was configured to control the GTAW power supply arc initiation and arc intensity. However, the PAW system required at least 7 channels to control various parameters for the experiments, as such it was impossible to use the Smoothieboard. Therefore, a DUET 2 Ethernet [76] control board along with the DUEX 2 Expansion board [77] were selected with an I<sup>2</sup>C communication port that allows controlling multiple devices. I<sup>2</sup>C is a serial communication protocol where a master device (the printer) can send a message to a slave device (a microcontroller controlling the PAW system ports) and

receive data [78]. The author performed the research and conceptualized the requirements (Shown on Figure 21) for interfacing the printer and the PAW system via I<sup>2</sup>C in addition to supervising a colleague for preparing the proof of concept and adoption of the new system. It is to be noted that the upgrade is compatible with the GTAW system.

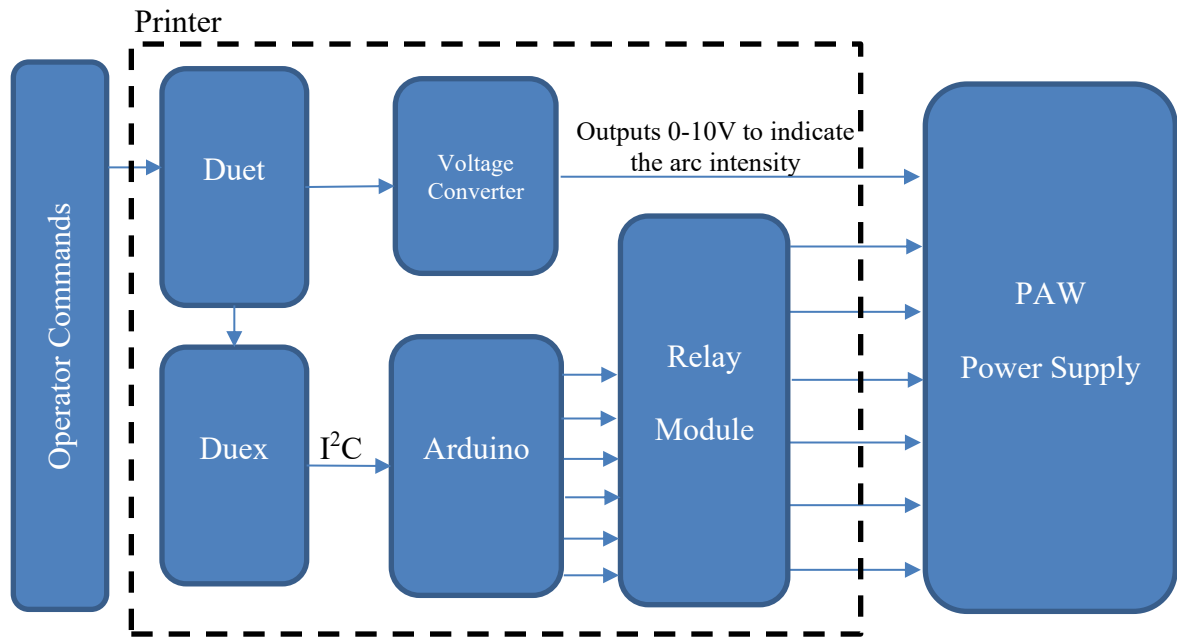
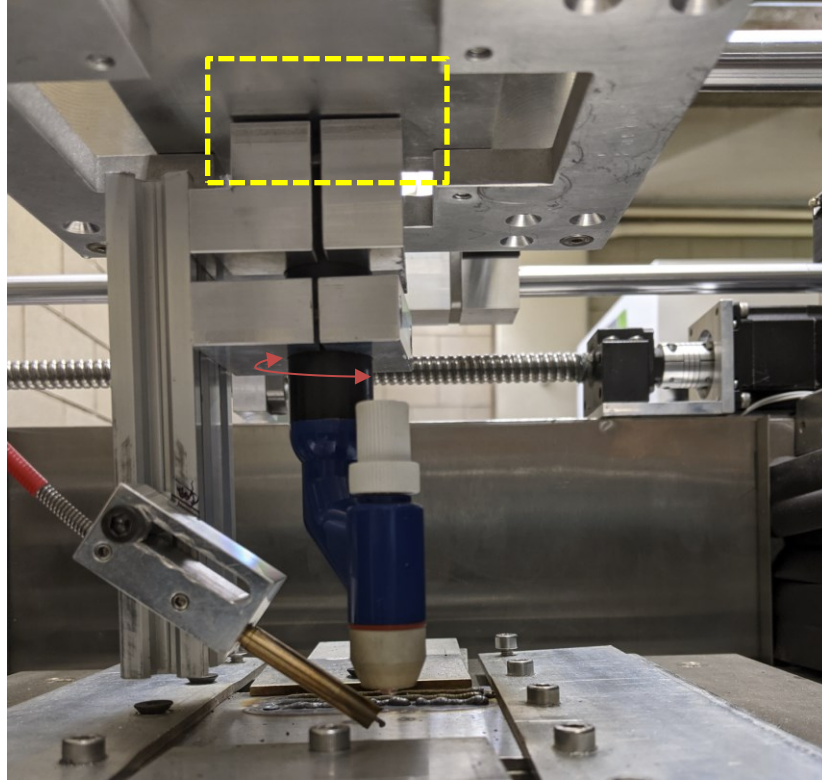


Figure 21: Conceptualization of the of the Printer interface with the PAW system.

### 3.6 Plasma Arc Welding (PAW) System Adoption

The implementation of a PAW system also required retrofitting of the printer with a new torch holder and a wire nozzle system which would benefit from adjustability and rigidity while reducing the calibration time.



**Figure 22: Torch holder and wire nozzle system designed for the PAW wire and arc additive manufacturing. The red arrow indicates the rotation of the torch along vertical axis.**

The PAW setup benefits from the GTAW research findings such as the ability to adjust the Nozzle outlet angle and location, high temperature stability, and ease of calibration, however, two major issues have since been identified with the design. First, the weight of the mechanism and vibration of the machine promote slippage of the holder from the dowel pins that support its weight. The gap must be removed as shown in the yellow dashed rectangle since the torch would not be perpendicular to the substrate. Secondly, the torch needs to be constrained along the vertical axis to ensure alignment of the torch and the wire. Figure 23 shows the calibration method that was developed to ensure Wire-Arc alignment. Once the substrate is installed and the wire is trimmed the torch should be brought to the arc-length position over the substrate and the arc turned on for few seconds,

and further adjustment should be performed based on the location of the wire strike on the semi-melted substrate.



**Figure 23: PAW torch calibration which should be performed until the wire is at the center of the circular marks.**

## **Chapter 4: Coordinated Heat and Feed Printing Strategy for Wire and Arc Additive Manufacturing of Metal-Cored Wires**

*This peer reviewed article was mainly written by the thesis author, Shahryar Shahryari Fard, but Dr. Hanspeter Frei, Dr. Xiao Huang, and Dr. Matthew Yao has performed the reading and editing for different iterations of the manuscript.*

### **4.1 Abstract**

Metal-cored wire provides material selection diversity for applications where there are no commercially available solid wires. This is becoming more desirable with additive manufacturing in particular. This paper investigates the application of a Stellite 6 metal-cored wire in a Wire and Arc Additive Manufacturing (WAAM) of thin-wall structures with a thickness of  $\sim 3.5$  mm using the Gas Tungsten Arc Welding (GTAW) process. Preliminary experiments by continuous travel of the GTAW torch and constantly feeding the wire showed an unreliable deposition of consecutive layers. A new method was developed featuring a Coordinated Heat and Feed (CHF) printing strategy. This method provided improved control of the weld pool and minimized the nonuniform spread of the molten material. The CHF printing strategy was implemented by dividing the print path into small segments, each of which underwent three sequential steps: i) the weld pool formation, ii) the wire insertion into the weld pool, and iii) the cooling of the molten pool. A 7-layer thin-wall structure fabricated by this CHF printing strategy was compared with a continuously printed specimen. The results showed that the CHF specimen presented a better geometrical quality and macrostructure uniformity. Both samples had similar microstructural features and properties.

## 4.2 Introduction

Additive manufacturing (AM) provides an unsurpassed ability to manufacture components with low manufacturing and material cost, higher material diversity, faster design-to-product turnaround time, and more freedom in design compared to conventional subtractive manufacturing processes [79]. Among the various categories of Metal AM, arc based processes such as the Gas Metal Arc Welding (GMAW), Gas Tungsten Arc Welding (GTAW), and Plasma Arc Welding (PAW) are considered to have the advantages of being simple and easy to operate while requiring less material usage since the feed-stock is in the form of wire as opposed to powder [47], [80]. These processes are termed more specifically as Wire and Arc Additive Manufacturing (WAAM). Usually WAAM yields lower quality products in terms of dimensional tolerances and surface finish, in comparison to processes using laser or electron beam combined with powder feed, due to intensive heat input and high material deposition rate [80], [81]. However, WAAM offers unique advantages such as lower equipment and material costs, better feedstock control, large selection of available materials and the use of tubular wire. The overall goal of our research is focused on the development of new WAAM processes with the goals to improve the print quality and reduce and ultimately eliminate the need of machining.

Thin-wall structures are of great interest to the manufacturers of AM components. There has been extensive research on manufacturing of thin-wall structures using WAAM and particularly GMAW is widely attempted to produce thin-walled structures. There are multiple variants of GMAW, but all utilize wire as part of the arc generation circuit and the source for the material deposits [82]–[87]. Panchagnula et al. [83] and Kazanas et al. [82] presented examples of thin-wall construction and discussed inclined walls and closed

shapes which were created with the GMAW based Cold Metal Transfer (CMT) method. Furthermore, extensive research has been conducted on thin-wall WAAM structures manufactured using GTAW [53], [88]–[91]. These studies showed that part quality produced by GTAW-AM was generally inferior compared with the CMT in which the wire is maintained perpendicular to the weld pool, whereas the wire orientation depends on the direction of travel in GTAW-AM [80], [89], [92]. Another factor contributing to the superior quality of the CMT is the reduction in heat input compared to the conventional GTAW method [93]. However, the dependency of minimum wall thickness in the CMT method on the diameter of the wire is a deterrent for adoption of this method for printing walls with low thickness [85].

Some studies described GTAW-AM experiments where welding power input was reduced by utilizing Hot-Wire Arc Additive Manufacturing (HWAAM) [88], or by means of current pulsing [53], [89], [90]. Resistance heating of the wire in HWAAM allows for the reduction of arc current, resulting in the improvement of the material properties while at the same time providing more control over the width of the deposits [88]. Resistive heating of the wire can potentially be implemented with many metal AM processes to reduce heat input. Pulsing the current in GTAW-AM, i.e., fluctuating the current between a base current and a peak current over the duration of a predetermined cycle, also enables the reduction of the overall heat input (i.e. increase the process efficiency) and therefore improving the microstructural properties of the weld bead [95]. During the base current period a molten droplet at the tip of the wire is formed and then transferred to the substrate once the arc reaches the peak current period [96]. Xu et al. [90] used this method to construct large scale lattice structures that can be used in ship deck building and aerospace industry. Each

pyramidal unit cell was comprised of 4 inclined rods (~5 cm long and ~5 mm in diameter) ranging from 30 to 90 degrees. Each rod was printed individually along predefined deposition directions whereas the diameter of the rods was controlled by the heat input. Composition of feed wires for WAAM is currently limited to commercially available wires developed primarily for welding [84]. The production of solid, homogeneous wires becomes cost prohibitive, if not impossible, with alloys that offer enhanced material properties such as wear resistance [97]. These advanced materials can be manufactured into metal-cored wires where metal powder mixtures are packed into a cylindrical, ductile metal sheath. Potentially, the metal powder can be any compatible material in the creation of new alloys. In this study, the objective is to print thin-wall (~3.5 mm width) geometries using a GTAW-AM with a 1.2 mm diameter Stellite 6 metal-cored wire (Kennametal Inc., Belleville, ON, Canada) under two different modes: constant current with continuous motion and a newly developed printing strategy. This paper reports the preliminary findings.

### **4.3 Materials and Methods**

#### **4.3.1 Experimental Setup**

A custom-built Computerized Numerical Controlled (CNC) machine equipped with a GTAW torch and a computer-controlled wire feeder (3D printer) were used in this study (Figure 24).

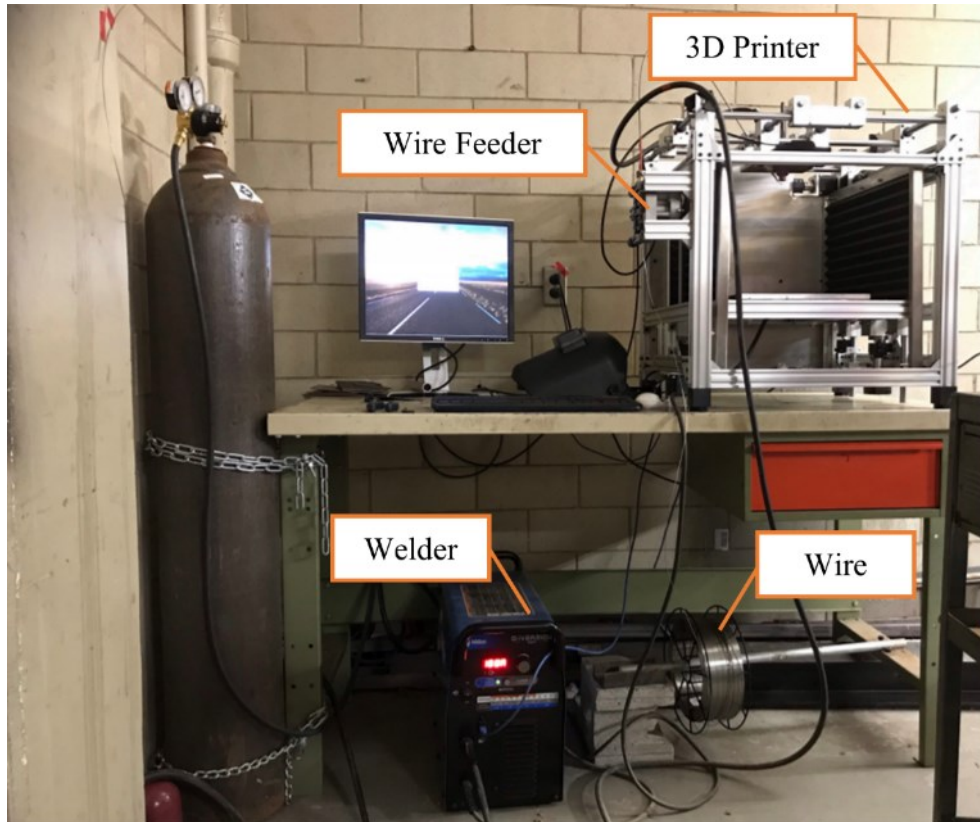


**Figure 24: Experimental setup for the WAAM research at Carleton University. The 3D printer is a custom build CNC machine with a computer-controlled wire feeder. The travel speed and direction, the welding current, and the wire feed are controlled independently.**

The initiation and termination of the welding arc and the wire feed, the welding current, and the wire federate was programmatically controlled during printing. As a result, various welding parameters were integrated with the travel pattern and speed. The welding power supply was a Miller Diversion 180 operating with 99.97% Argon and a 1.6 mm Lanthinated Tungsten electrode. All the experiments in this research have been conducted with the torch oriented perpendicular to the substrate.

Table 2 provides the composition of Stellite 6 which is commonly used in the valve industry as a high temperature wear resistant alloy [98].

**Table 2: Composition of Stellite 6 metal-cored welding wire (wt.%) (Ref 22)**

Co	Cr	W	C	Ni	Mo	Fe	Si	Other
Bal.	30	4.5	1.2	<3.0	<1.0	<5	<2.0	<1.0

Thick 304 stainless steel plates (3.175 mm thickness) were used as the substrate. They were thoroughly sandblasted and were clamped to the printer bed. The post print metallurgical analysis was conducted based on established protocols of sectioning and polishing. First, the samples were divided into smaller sections using a band-saw allowing which allowed the sectioning on an abrasive saw. After cutting, the specimens were mounted using Bakelite. Etching of the specimens was performed with Kalling's II etchant. The acquisitions of micrographs and the Energy-Dispersive X-ray spectroscopy (EDX) analysis were performed by the Tescan Vega-II XMU scanning electron microscope on Carbon-coated mounted specimens, A Vickers Hardness tester from Clemex Technologies Inc. was utilized to measure the hardness value for the specimens. The hardness value reported for each layer of the specimens in Section 4.4.3 was the average of 7 measurements for the respective layer.

#### **4.3.2 Conventional GTAW-AM**

In the conventional GTAW-AM method, similar to that reported in references [41], [92], [99], [100], a constant current (non pulsing current) heat source continuously travels over the path as the wire is added with a constant feed rate. The trials for printing with Stellite 6 wire were initiated based on our previous work [42] for a solid wire with the similar setup. Single layer beads were achieved after slight modifications, and the parameters for subsequent layers were found by experimentation. However, this process did not produce acceptable thin walls (~ 3.5 mm) as explained in the results (Section 4.4.1, Figure 27). After further experimentation, a 7-layer wall was eventually printed by continuously

moving the arc and a constant wire feed over a 60 mm straight line where wire led the arc. It was found that a travel speed of 80 mm/min and a wire feed rate of 210 mm/min worked best in this application. The Argon flowrate was controlled at 25 CFH and fed into the system through a gas lens to increase arc stability. The current was set to 68 A for the first layer. For the second and third layers, the current decreased by 28% and 14% respectively. The fourth layer was deposited with a 7% reduction in current, whereas the rest of the layers were deposited with a current of 37 A (reduction of 5% compared to layer 4). After each layer, the height of the specimen was measured with a caliper to ensure that the subsequent layer was printed at a constant arc length of 3 mm. Between each layer, measurements took about 2 to 3 minutes while allowing for cooling of the specimen.

#### **4.3.3 Coordinated Heat and Feed Printing Strategy**

Challenges encountered in printing experiments with conventional GTAW-AM methods resulted in the development of a new WAAM printing strategy. The new Coordinated Heat and Feed (CHF) was implemented by dividing the planed print path into small path segments, each of which underwent 3 different sequential steps: i) the weld pool was formed, ii) the wire was inserted into the weld pool, and iii) weld pool was uniformly solidified by adding filler material. Figure 25 illustrates the setup along with the terminologies that were used to describe the method. The main advantage of the new strategy is the additional control over the intensity and timing of heating and cooling. The energy input can be potentially minimized and therefore increasing the efficiency of the process. Implementation of the CHF printing strategy for the Stellite 6 metal-cored wire is illustrated in Figure 26.

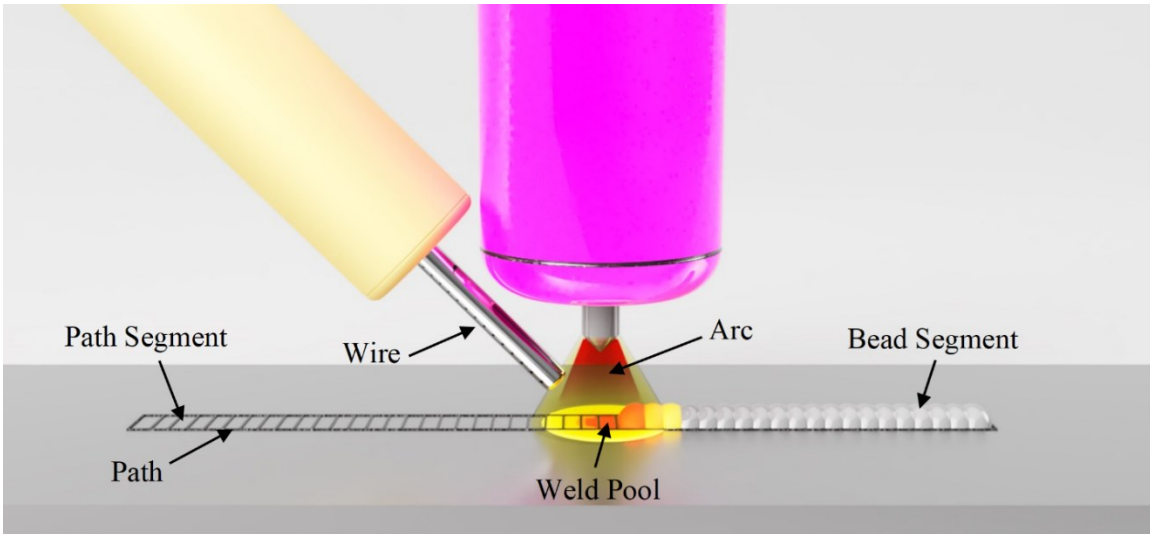


**Figure 25: Computer rendered schematic showing weld pool formation, the first step of the CHF deposition process and the related terminologies.**

For printing a 7-layer Stellite 6 wall, the steps were implemented as per the following:

*i) Forming the weld pool:* as shown on Figure 26b, creation of the weld pool was initiated by the activation of the high current which persisted for a specified amount of time (450  $\mu$ s).

*ii) Inserting the wire into the weld pool:* the overall designated length of the wire for each bead segment was 3.5 mm, i.e. 50% of it inserted into to weld pool during the high current as illustrated by Figure 26c. The rest of the wire was inserted into the weld pool during the low current heat setting as shown on Figure 26d. Once the full length of the wire was inserted, step ii) for the CHF printing strategy is complete. Given the chosen parameters, the tip of the wire returned to its original location after melting in the weld pool.

*iii) Uniformly solidifying the weld pool with the filler material added:* the current was reduced to the low state following the high current for a predefined amount of time (500  $\mu$ s) to assist in cooling down the bead segment (as shown on Figure 26e).

The same steps were repeated for the next path segments. A summary of the parameters utilized for printing a 7-layer CHF wall is provided in Table 3 where the unreported parameters are identical to the conventional method. These parameters were selected based on various trials while observing the melting behavior of the wire during the print. Further studies and provisions are required to further optimize these parameters.

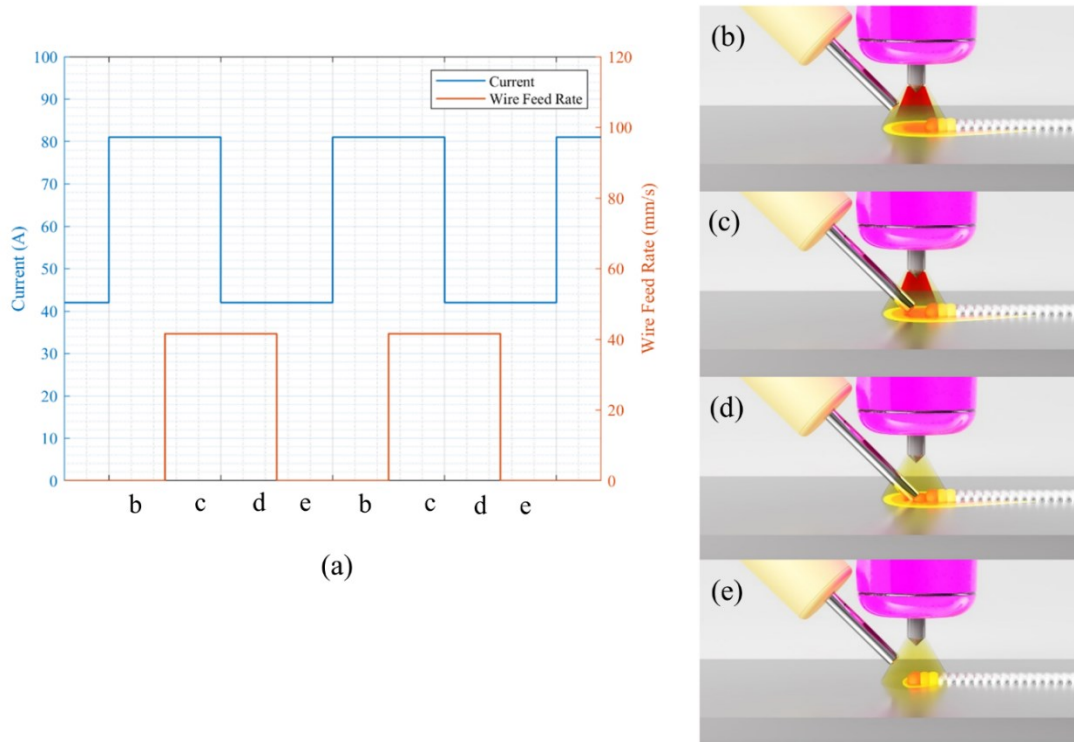


**Figure 26: The illustration of the Coordinated Heat and Feed (CHF) printing strategy for Stellite 6. a) Behavior of the current and wire feed rate for two consecutive path segments. b) – e) Schematic of the wire, weld pool, and the deposits according to the label on a).**

**Table 3: 7-layer CFH specimen running parameters**

Variable	Layer 1	Layer 2	Layer 3	Layer 4	Layer 5	Layer 6	Layer 7
High Current (A)	81	58	50	46	44	44	44
Low Current (A)	42	30	26	24	23	23	23
High Current Duration (ms)	450						
Low Current Duration (ms)	500						
Length of wire inserted for each bead segment (mm)	3.5						
Wire feed rate (mm/min)	2500						
% of wire inserted during high current	50%						
Length of each path segment (mm)	1						
Electrode distance to the metal surface (mm)	3						
Ar Gas flow rate (CFH)	25						

#### 4.4 Results and Discussion

##### 4.4.1 Conventional GTAW-AM

The initial experiments demonstrated that GTAW-AM with metal-cored Stellite 6 wire produced unreliable and inconsistent base layers (i.e. the first layer), even when the same welding parameters were used. As shown by the rectangles on Figure 27, the base layers deviated from straight lines and had uneven bead heights. These base layers were inadequate to form the basis for subsequent layers due to inconsistent dimensions hence inevitable changes in the arc length. Additionally, the nonuniform spread of the material, shown by the circles in Figure 27, contributed to the dimensional inconsistency of the conventional method. The nonuniform height caused by uneven and random spread of the

material negatively affected the repeatability of the process. Bead width and height would be expected to be proportional at any location along the bead since the wire feed rate was kept constant throughout the deposition. The bead height was lower at locations where the molten material was spread over a larger area which influences the arc length and the overall heat input if a subsequent layer were to be added.

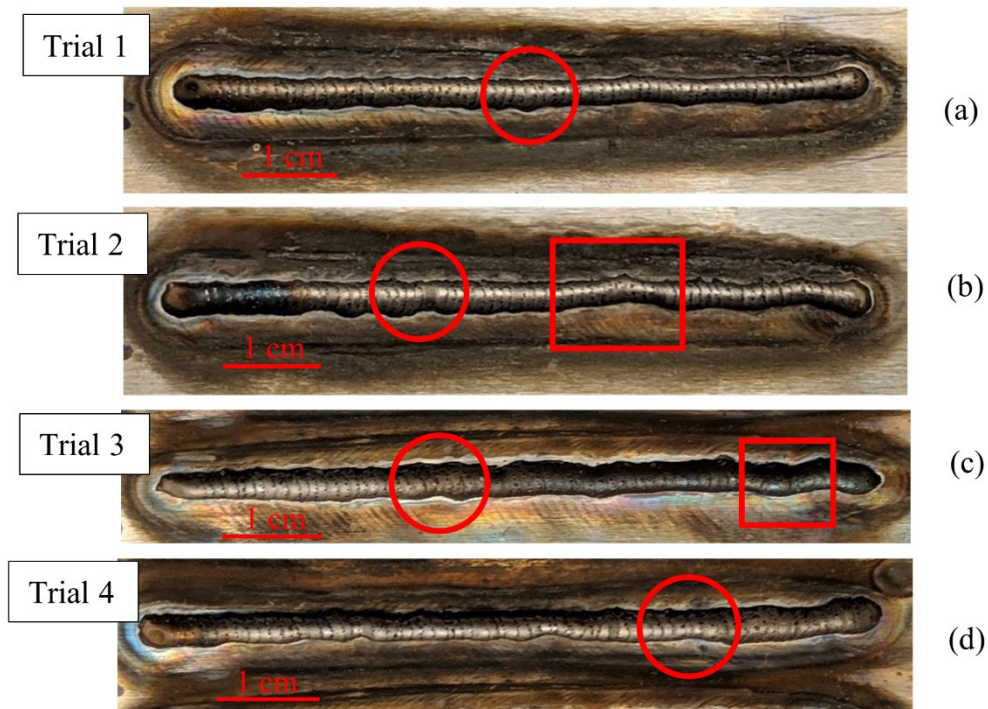


**Figure 27: Single layer beads using the conventional GTAW-AM method with identical printing parameters for all the trials. The base beads were unreliable and insufficient for subsequent layer deposition. The rectangles show instances where the deposition deviated from the path which negatively affected deposition of subsequent layers. The circles indicate the uneven spread of molten material that directly affect the height of the bead at the corresponding locations.**

The path deviation and uneven spread of the material were attributed to the formation and transfer of the molten droplet to the weld pool. It was observed during the process that the

wire was melted by the arc, before reaching the weld pool, in a shape of a droplet and grew as wire feed continued. Once a specific size was reached, the molten droplet fell off the wire into the weld pool. Any deviation to the arc could disrupt the formation of the droplet and caused changes in droplet size, location, and timing of the drop on the planned path. Additionally, the uncontrolled fall of the droplet onto the weld pool could potentially be the reason for the uneven spread of the material. A remedy to this issue was to eliminate the droplet formation and transfer away from the weld pool; that is to melt the wire at the weld pool. To achieve this goal, the wire feed rate must be increased to a level so that the wire was always in contact with the weld pool throughout the printing process. Unfortunately, the resulting wall thickness would have been much wider than the set goal. Despite the issues with the consistency of the conventional method, the 7-layer wall was printed and is shown on Figure 28. The issues discussed above were evident. The undulating pattern on top of the wall resulted from the nonuniform heat input due to uneven spread of the material, and the sharp cavity on the wall was formed because of an undesired print path deviation. The average height of the 7-layer specimen, measured from the plane of the substrate, reached 7.40 mm excluding the corners and the visible cavity. The average thickness of the conventionally printed specimen was 3.30 mm.

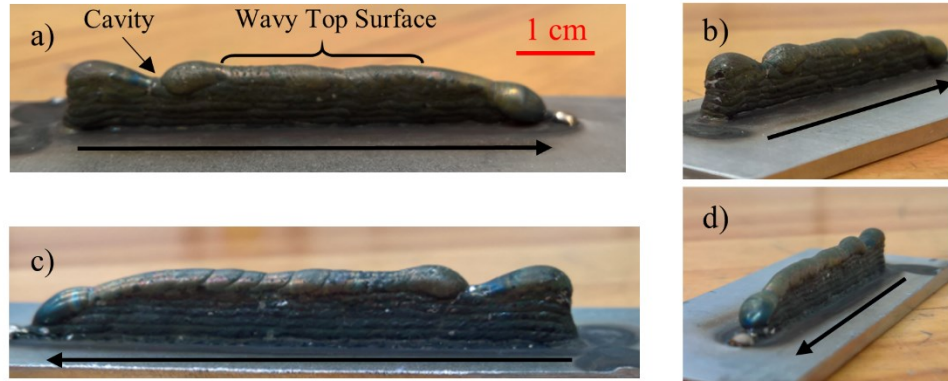


**Figure 28: The continuously printed specimen. Arrows indicate the printing direction. a) Front view. b) Oblique view from the front. c) Back view of the sample. d) Oblique view from the back. The wavy top layer was a result of uneven spread of the material and change in the heat input. The cavity was caused due to the deviation of the deposit from the planned path.**

#### **4.4.2 Coordinated Heat and Feed Printing Strategy**

The CHF method substantially improved the print quality and repeatability of thin walls with Stellite 6 metal-cored wires as shown in Figure 29. The height of the 7-layer deposition without considering the corners was measured to be 7.50 mm, and the average thickness was 3.20 mm.

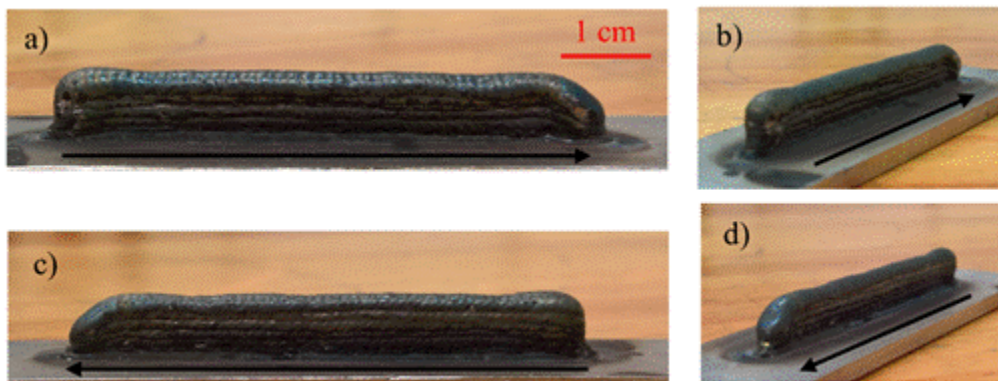


**Figure 29: The CHF specimen. Arrows indicate the printing direction. a) Front view. b) Oblique view from the front. c) Back view of the same sample. d) Oblique view from the back of the same sample.**

No uneven spread of the material or path deviations were observed as the wire was constantly melted in the molten pool. Each of the three steps in the CHF printing strategy contributed to the improved quality of the wall:

*i) Forming the weld pool:* CHF allowed the creation of a consistent weld pool which was key to achieve a uniform deposition. The geometry of the deposited bead and the weld pool could be controlled with the welding parameters such as current, travel speed and wire feed rate [101], [102]. The time that the arc was held stationary at a given path segment affected the weld pool size and solidification time. The delay in solidification was assisted by longer heating time and allowed the cold wire to be inserted into the molten pool and to melt.

*ii) Inserting the wire into the weld pool:* Consistent melting of the wire within the weld pool at each path segment was critical to ensure the geometrical uniformity of bead segments. The wire was inserted when the heat source was stationary which enabled the addition of a constant amount of wire to each path segment. Furthermore, the CHF printing strategy could potentially be used with multiple types of wires, even with different melting temperatures. The wire may be inserted at any given, but predetermined moment with any pattern (e.g. 2 mm inserted, 1 mm retracted, and then 1 mm inserted) while a specific bead segment is being formed. The amount of wire being fed into the weld pool controlled the effective cooling rate at each path segment which can affect the mechanical properties of the finished product [96]. Weld pool dilution can be a potential disadvantage of the required high speed wire insertion into the weld pool (Section 4.4.3).

*iii) Uniformly solidifying the weld pool with the filler material added:* The final step was to cool down the deposited material at each segment. This could be achieved by optimizing

the amount of wire inserted and/or by holding the welding torch with reduced arc current over the deposited material while allowing the shielding gas to aid the cooling. The aim of this step was to cool down the newly deposited bead segment to a condition of the respective path segment prior to the start of step i). This step is implemented in fact in preparation for the deposition of the next bead segment.

Li et al. [53] fabricated a hollow cube from the Stellite 6 metal-cored wire with a wall thickness of about 1 cm using a pulsing GTAW-AM method. Wilson [103] reported on a modified GTAW process, TIP TIG, in which a secondary oscillation of the wire improved the deposition speed and quality of the bead. Furthermore, Silva et al. [104] combined this method with pulsed GTAW and concluded that the weld beads were symmetric and the process was more robust compared to conventional methods. Even though the authors have not been aware of any research implementing the TIP TIG (with current pulsing) for wire and arc additive manufacturing, there are common features between this method and the CHF deposition strategy examined in our study. The melting of the wire in the weld pool and the decreasing of the heat input by means of pulsing the current are common among both methods. However, the CHF printing method provided more control over the geometry of the deposited material as each segment of the bead was created with the heat source at a standstill. This characteristic of the process potentially allows for an improved control for creation of different geometrical features such as rounds, chamfers, and edges. Moreover, the CHF printing strategy ensured melting of wire by the weld pool as opposed to the arc. At each path segment, the high current arc creates a weld pool. While the wire was inserted at the speed of 2500 mm/min, the arc current is substantially reduced allowing the wire to be inserted into the weld pool under low current. This eliminates the droplet

formations caused by the arc at the wire tip. Droplet formation resulted in uneven and poor-quality deposits when using the conventional printing approach. Through visual inspection we were able to confirm that droplet formation was almost eliminated with our new technique and the wire remained in contact with the weld pool when desired.

#### **4.4.3 Material Properties and Comparison of the Specimens**

The microstructure of the two specimens was compared and no major variations were observed. Figure 30 illustrates the microstructure of both samples at the boundary of layer 5 and 6. As the boundary was not obvious, dashed red lines were added to Figure 30 to delineate the boundaries in both samples. In Addition, slight aggregation of Chromium Oxide (darker particulates on the microstructure) marks the location of the layer boundary. Figure 31 illustrates the EDX results for a dark spot at the boundary between layers 6 and 7 of the conventionally printed specimen. Abundance of Chromium showed the nature of these particulates, however, the detection of other elements indicated that elements from the surrounding area were also measured due the thinness of these particles. Further observation along the layer boundary for both samples indicated partial re-melting of the preceding layer during the deposition of the successive layer. This is a desirable feature as layer boundaries, if not properly fused, accentuate the anisotropic properties associated with AM of metallic materials, and the direction perpendicular to the boundaries often exhibited lower ductility as shown in many previous studies [66], [105].

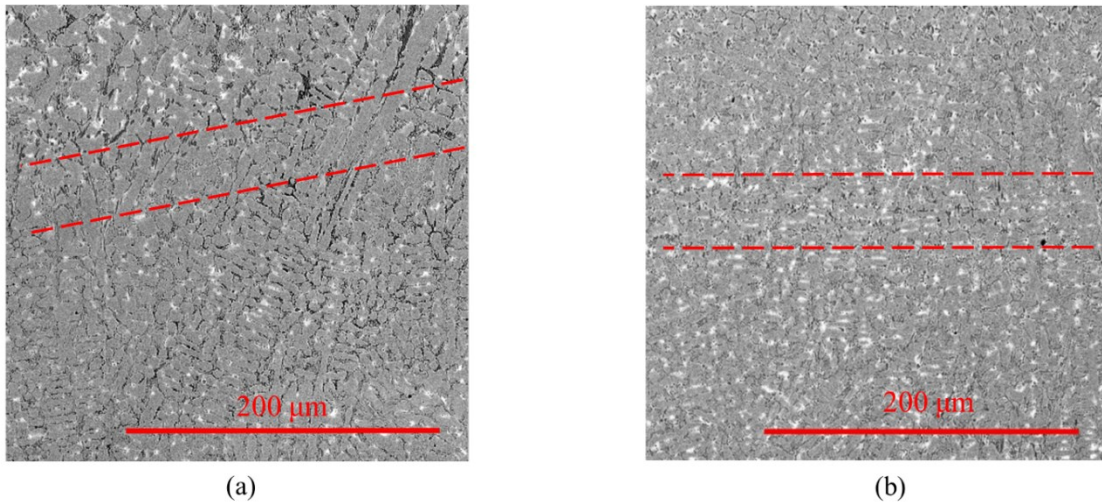


**Figure 30: SEM micrographs of specimens at the boundary of layers 5 and 6 where there is a uniform distribution of the microstructural features. (a) The conventionally printed specimen. (b) The CHF specimen. The dashed red lines indicate the boundary between the layers.**

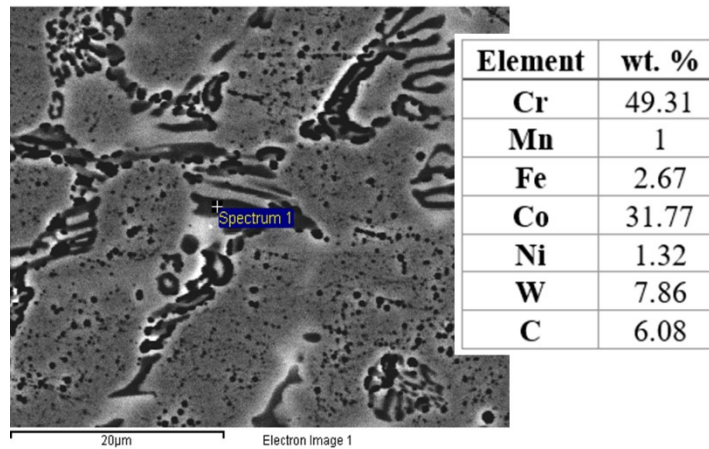


**Figure 31: EDX analysis of a dark particulate at the boundary of the 6th and 7th layer of the conventionally printed specimen. Figure was obtained by randomly zooming into the boundary area.**

Furthermore, tungsten rich particulates, as bright spots due to its high atomic number, were observed consistently across the microstructure (white spots in Figure 30 and Figure 32).

Figure 32 further illustrates two large bright particles at layers 1 and 7 of the conventionally

printed sample. Although it is not completely certain regarding the source of these bright particles, two possibilities are proposed. The presence of large Tungsten particles in the powder mixture within the wire sheath could be a reason behind this observation. The second source was speculated to be due to the melting of Tungsten electrode which is common during GTAW. However, the EDX data did not fully support this possibility as Lanthanum was not detected (referring to the type of the electrode detailed in Section 4.3.1).

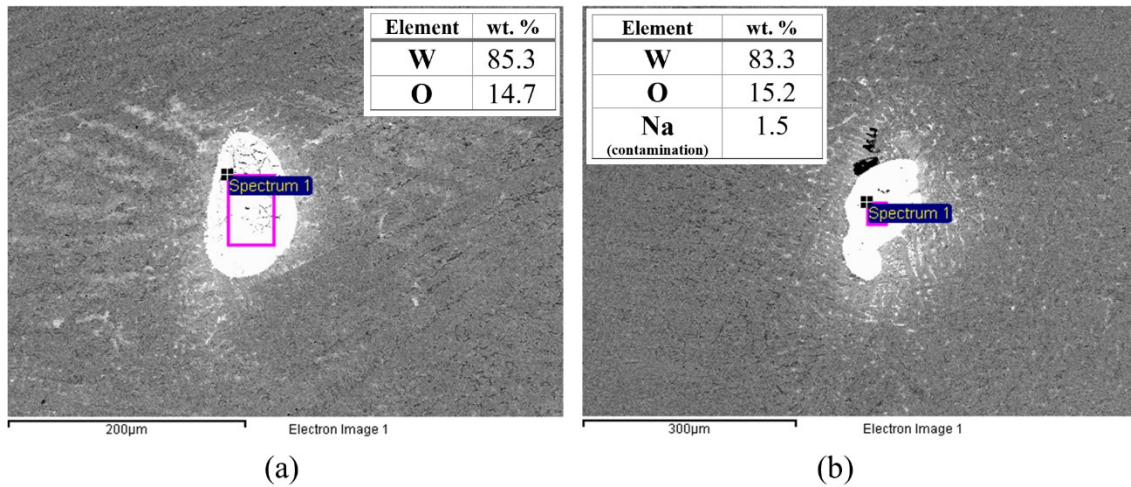


**Figure 32: SEM micrographs and EDX results of the large Tungsten particles in the (a) 1st layer, and (b) 7th layer of the conventionally printed specimen. The insert windows indicate the area for the EDX analysis.**

Further inspection of the microstructure of both samples revealed an interesting observation which is unique to GTAW-AM of metal-cored material when printing low thickness walls with low heat input. It was found that the sheath was not completely melted/mixed with the powders in the core during the deposition. Although not categorized as a defect, it contributes to slightly different composition from region to region. As this

occurrence presents mostly close to the edge of both specimens, post AM machining would presumably remove it effectively. In the interior of the wall thickness, since the heat density is far greater as it is closer to the centerline of the electrode (which is colinear with the centerline of the deposition), the incomplete melting/mixing was not observed. Figure 33 illustrates the area with primarily metal sheath composition (spectrum 1) on layer 5 of the CHF specimen along with the selected areas corresponding to the EDX data presented in Table 4.

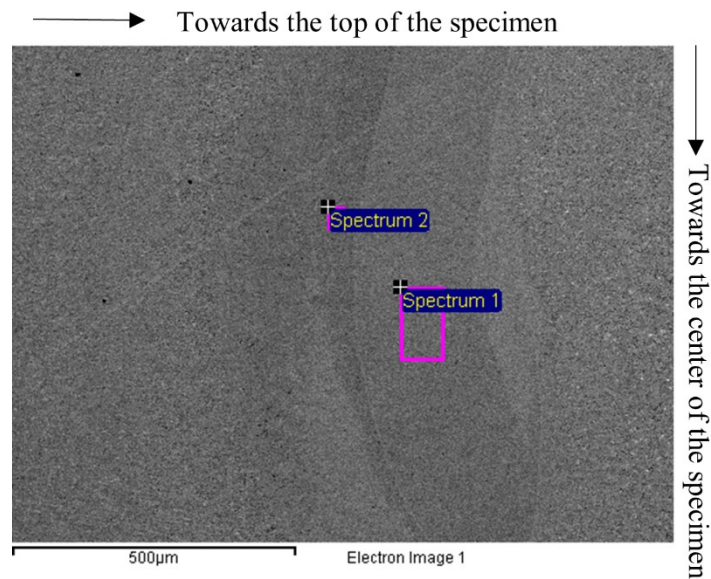


**Figure 33: The SEM micrograph of the unmelted/unmixed wire sheath in the 5th layer of the CHF specimen. The pink lines represent the detection areas for EDX analysis in which the data have been recorded in Table 4.**

**Table 4: Composition of the defect and its surrounding on layer 5 of the CHF specimen**

Element	Spectrum 1 Composition (wt.%)	Spectrum 2 Composition (wt.%)
Fe	5.82	4.45
Co	88.74	70.91
C	5.44	0.76
O	-	0.4
Si	-	0.57
Cr	-	16.79
Mn	-	1.03
Ni	-	3.13
W	-	1.96

As indicated in Table 4, the composition in spectrum 1 is a mixture of Cobalt and Iron which are the constituting elements of the sheath of the Stellite 6 metal cored wire. The composition of the material outside of the “sheath” area (Spectrum 2) was closer to that of Stellite 6, because the large amount of Cr detected (not in the sheath). This type of “defect” was observed in both specimens, irrespective of deposition methods used. However, these defects are less likely to be present in the GMAW-AM methods (such as CMT) in which the heat density of the arc is focused on the sheath of the wire. In addition, as opposed to the conventional method used in this investigation, GTAW-AM experiment with large amount of heat to melt the wire are less susceptible to this type of “defect”. Figure 34 represents the layer-by-layer hardness comparison of the specimens. The CHF specimen demonstrated a slightly higher hardness value which can be justified by the faster cooling rate (and potentially smaller grain size and more residual thermal stress) that was embodied in the process [86]. The large error bars on the data points could be attributed to the presence of intermetallic particles such as those presented in Figure 32. In addition, the

CHF strategy seems to yield samples with more consistent hardness distribution. The average hardness for the CHF sample ( $491 \text{ HV} \pm 67 \text{ HV}$ ) is similar to the range of average hardness (440-470 HV) reported in [53], therefore, the tensile strength could be near or slightly above the reported the reported values.

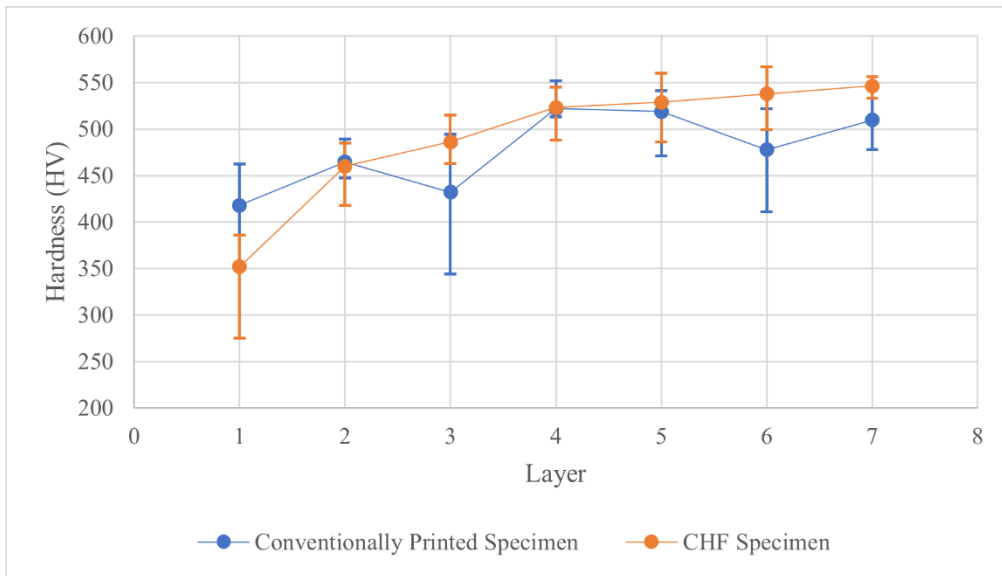


**Figure 34: Layer-by-layer hardness value for both specimens. Each data point is a numerical average of 7 data points on each layer and the error bars indicate the range of the collected measurements.**

As discussed previously, the periodic insertion of the wire into the weld pool may cause unwanted disturbance to the weld pool and introduce dilution of the substrate within the Stellite 6 alloy due to the molten fluid flow. As shown in Figure 35 are the composition profiles of Co, Fe, and Cr for both samples based on a layer-by-layer EDX analysis. The mixing of the substrate with Stellite 6 can only be observed in the first two layers of the CHF specimen. The low hardness in the first two layers (as shown in Figure 34) could be attributed to the change in the composition. Even though in many applications the substrate and the first few layers would be removed, the CHF method can be further tuned to reduce the dilution of the substrate.

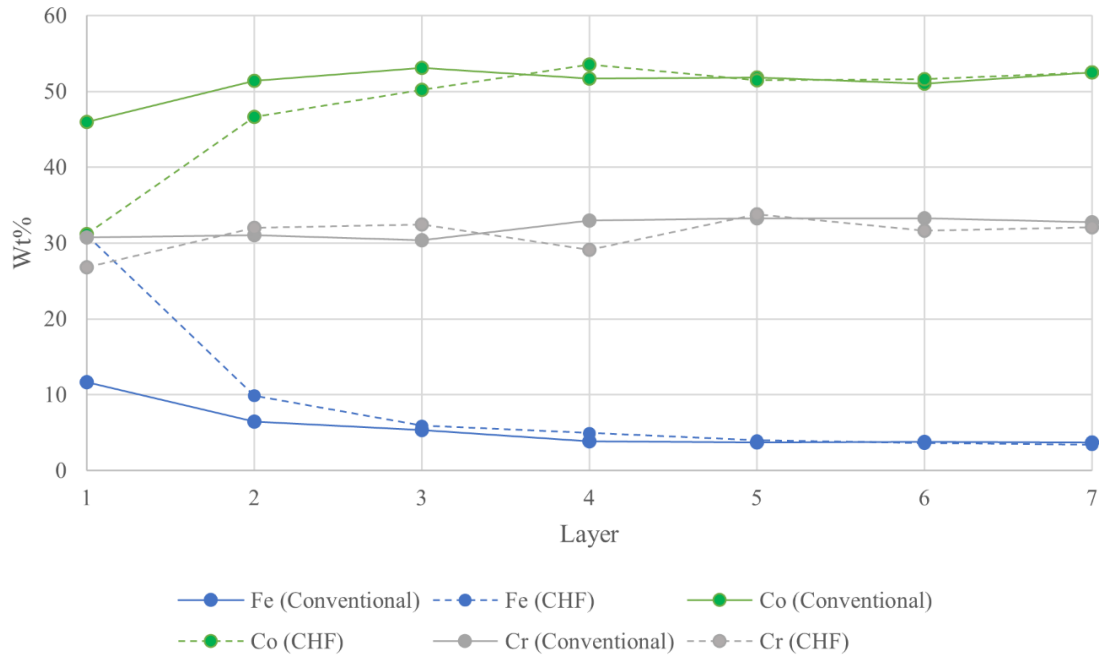


**Figure 35: Layer-by-layer composition of Co, Fe, and Cr for both samples extracted from EDX analysis of the specimens. The drop in the composition of Fe from first to second layer indicates that the effects of substrate-dilution disappear.**

#### 4.5 Conclusion

This paper presented a new GTAW-AM process for manufacturing of a thin-wall structure (~ 3.5 mm) using a metal-cored wire. Published, conventional printing methods of GTAW-AM were found to be unreliable for producing thin-wall structures. The newly developed Coordinated Heat and Feed (CHF) printing strategy allowed more control over the melting of the wire and the cooling of the weld pool by dividing the path into segments. A weld pool is created for each segment, the wire is then inserted, and finally the deposited material is cooled. These steps are repeated for all the path segments until a uniform bead, consisted of multiple bead segments, is achieved. The new strategy was further evaluated by comparing the macrostructure, microstructure, and material properties between a

conventionally printed 7-layer sample and a 7-layer sample fabricated with the CHF printing strategy. The CHF method produced a uniform macrostructure as opposed to the conventional method which presented irregular deposition shape resulting in ununiform dimension and shape of the specimen. Nevertheless, the microstructure of both specimens remained similar although the CHF specimen displayed higher and more uniform hardness from the perspective of material properties.

#### **4.6 Acknowledgements**

The authors would like to acknowledge the financial support from the Natural Sciences and Engineering Research Council of Canada (NSERC) Engage Grant No. EGP 530790-18.

## **Chapter 5: Investigation on WAAM of Stellite 6 Metal-cored Wire with PAW**

### **5.1 Introduction**

As discussed in Section 2.1, the mechanical engineering industry benefits from Metal Additive Manufacturing (Metal-AM) in terms of reduced material consumption and fast turnaround. The low-cost processes such as arc-based AM provide more accessibility, although the components made by the more common arc-based AM processes (GMAW-AM and GTAW-AM) require further machining to improve the accuracy and minimization of stress concentrations. Little research has been conducted to achieve low thickness (<3.5 mm) thin-walls which could significantly reduce stair-stepping, improve accuracy, and may allow net-shape manufacturing. Posch et al. [94] reported that the minimum possible wall thickness with GMAW-AM is 4 to 5 mm when a 1.2 mm wire is utilized, therefore, the GMAW-AM would not be suitable for low thickness walls.

Plasma Arc Welding Additive Manufacturing (PAW-AM) is a type of Metal-AM where the heat source has been categorized as a High-Power Density process [106]. However, there have been less studies on its utilization for Metal-AM compared with GMAW-AM and GTAW-AM [107]. In general, the high penetration depth of PAW in AM is not a good characteristic as it causes excessive remelting of the preceding layers and leads to defects [108]. Martina et al. [109] utilized PAW for maximizing the deposition rate which resulted in creation of thick walls, however, the feasibility of printing low thickness walls was not explored.

The goal of our WAAM researchers at Carleton University is to explore if PAW can be utilized for minimizing the thickness of printed walls and improve the surface finish perpendicular to the deposition direction. This chapter contains the preliminary results for PAW-AM with Ø1.2 mm Stellite 6 metal-cored wire. There is currently no publication on PAW-AM using metal-cored wires.

## **5.2 Experimental Setup and Procedure**

### **5.2.1 Experimental Setup:**

The same printer discussed in Sections 3.3 and 4.3.1 was utilized for moving the PAW torch and the wire over a 3 mm thick 304 Stainless Steel substrate. As shown on Figure 36, the PAW power supply is a MIG-O-MAT plasmaJET100SPS equipped with a PJB100superior-M torch with 100% duty cycle. 99.97% purity Argon was used for both the shielding and plasma gas regulated to 3.5 bar specified by the manufacturer. Travel speed and direction, wire feed rate, arc (and gas) initiation and termination, and the arc current are controlled through the printer, whereas the nozzle-electrode gap, the shielding and plasma gas flowrates, and the plasma pilot characteristics are set on the PAW system. Metallurgical sample preparation along with the Scanning Electron Microscopy (SEM) were similar to that described in Section 4.3.1.

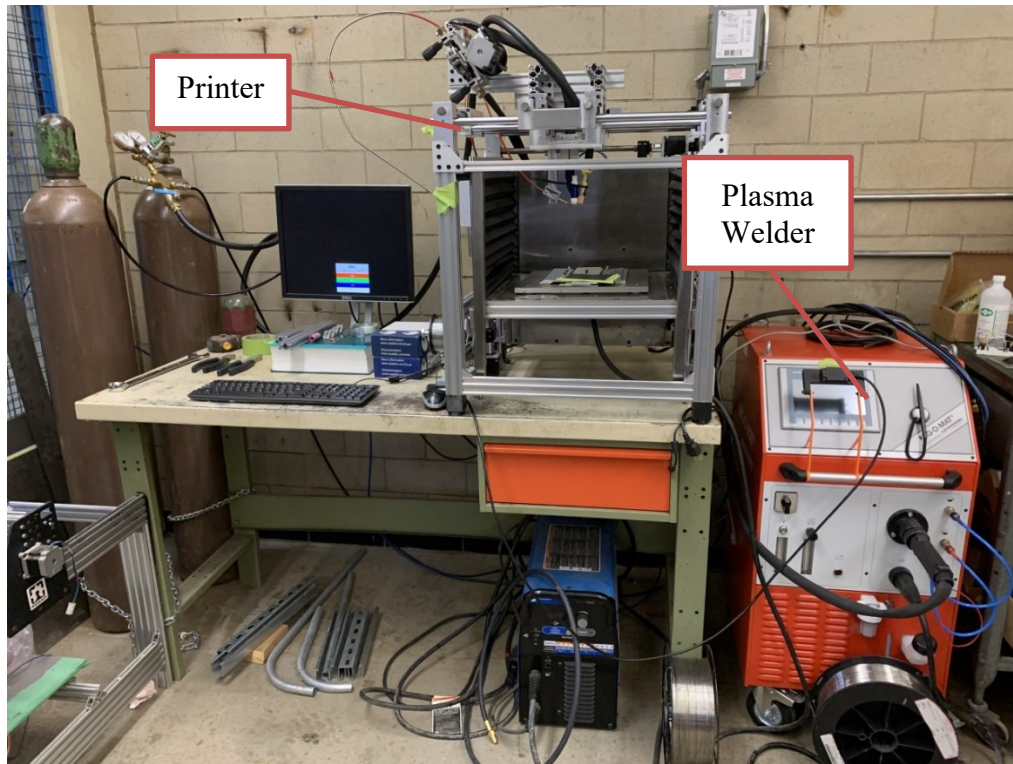


**Figure 36: Experimental setup for PAW-AM at Carleton University**

A characteristic of the PAW is the narrow plasma arc compared to the GTAW. If the narrow arc produces a bead-width weld pool with small partially-melted zone, as shown on Figure 37b, the melted filler metal can potentially spread over the previous bead with a better bonding. On the other hand, the plasma arc has a larger heat density ( $\text{W}/\text{cm}^2$ ) compared to GTAW and the melting of the wire occurs faster causing wire-arc misalignment and oscillation (see Section 3.3.1.2). To accommodate a continuously aligned wire feeding while creating a deep but narrow weld pool, it was decided to use a 1 mm plasma nozzle which is smaller than the wire.

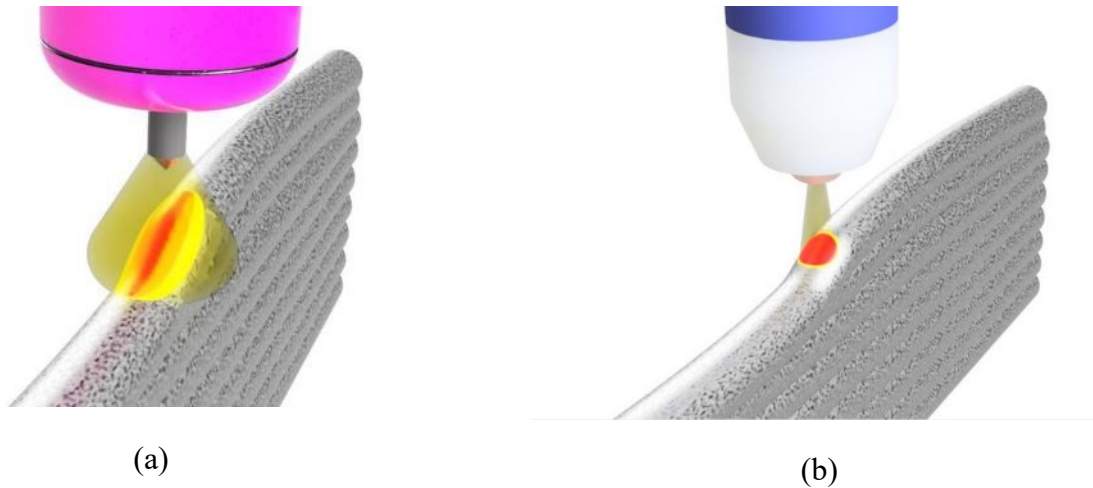


**Figure 37: Illustration of the weld pools created based on a) GTAW, b) PAW**

## **5.2.2 Experimental Procedure**

The goal of this phase of the study was to replicate similar 7-layer thin walls with the conventional method and the Coordinated Heat and Feed (CHF) printing strategy (explained in Section 4.3.3) using the 1.2 mm Stellite 6 metal-cored wire.

## **5.2.3 Preliminary Experiments**

The experiments began by conventional printing where the relationship between arc length, the minimum  $L_{\text{from Nozzle}}$  (the distance from the wire nozzle outlet to the weld pool as described in Section 3.3), wire nozzle angle and location were studied which led to the development of the calibration method described in Section 3.6. The final wire-arc relative position is shown on Figure 38 where the arc length is 10 mm, and the wire angle is 39 degrees.



**Figure 38: Final configuration of the wire and the torch for PAW-AM experiments.**

All trials were run with the plasma gas flowrate=0.25 L/min and a shielding gas flowrate=10 L/min while the pilot current was set to 12 A. After the ignition of the main arc, between 2 to 3 s of delay was considered before the initiation of printing to ensure the arc stability and sufficient heating of the electrode. The printing parameters for each trial are provided in the figure captions unless noted otherwise. Furthermore, the oxidation on the top surface of the beads was studied by measuring the oxygen content using an Energy-Dispersive X-ray spectroscopy (EDX) on top of the samples that were not polished. The oxygen content of distinguishable shades of grey was measured at two different locations over the bead surface, and the average was reported. However, the preliminary experiments indicated the shortcomings of the conventional printing method which resulted in abandonment of the conventionally printed 7-layer specimen. Instead, the CHF method was utilized with 2 different heating parameters while keeping the wire input constant.

**Table 5: Printing parameters the surface oxidation analysis.**

	Sample 1	Sample 2	Sample 3	Sample 4
High Current for Layer 1 (A)	28	20	-	28
Low Current for Layer 1 (A)	7	5	-	7
High Current for Layer 2 (A)	-	-	-	16
Low Current for Layer 2 (A)	-	-	-	6
Current for Conventional Printing (A)	-	-	28	-
Travel Speed for Conventional Printing (mm/min)	-	-	90	-
High Current Duration (ms)	450	800	-	450
Low Current Duration (ms)	450	450	-	450
Length of wire inserted for each bead segment (mm)	4.5	4.5	-	4.5
Wire Feed rate (mm/min)	2700	2700	270	2700
% of wire inserted during high current	100	100	-	100
Length of each path segment (mm)	1	1	-	1
Plasma nozzle outlet distance to the metal surface (mm)	10	10	10	10
Shielding gas flowrate (Lit/min)	0.25	0.25	0.25	0.25
Plasma gas flowrate (Lit/min)	8	8	8	8

#### 5.2.4 CHF Specimens

The CHF method developed for GTAW-AM consists of 3 steps which can similarly benefit PAW-AM. As discussed in Section 4.3.3, CHF ensures that a weld pool is created first, before insertion of the wire, and that a uniform solidification of the filler material in the weld pool takes place. Table 6 provides the parameters for printing the two 7-layer specimens using the CHF method. The first layer for specimen B was printed with the same configuration as the first layer of specimen A. However, after the first layer, the parameter changes as detailed in Table 6.

**Table 6: Printing parameters for the PAW-AM CHF samples.**

	Specimen A	Specimen B
High Current for Layer 1 (A)	28	<b>All parameters</b> identical to Layer 1 of Specimen A
Low Current for Layer 1 (A)	7	
High Current for Layer 2 (A)	17	16
Low Current for Layer 2 (A)	6	6
High Current for Layer 3 (A)	15	13.5
Low Current for Layer 3 (A)	5	5
High Current for Layer 4, 5, 6, and 7 (A)	14	13.5
Low Current for Layer 4, 5, 6, and 7 (A)	5	5
High Current Duration (ms)	450	750
Low Current Duration (ms)	450	450
Length of wire inserted for each bead segment (mm)	4.5	4.5
Wire Feed rate (mm/min)	2700	2700
% of wire inserted during high current	100	100
Length of each path segment (mm)	1	1
Plasma nozzle outlet distance to the metal surface (mm)	10	10
Shielding gas flowrate (Lit/min)	0.25	0.25
Plasma gas flowrate (Lit/min)	8	8

Specimen B was printed with a longer duration of high current to study the adhesion of the layers and microstructural differences. Repeatability of specimen A parameters was confirmed by printing 3 similar specimens of identical geometrical features. The delay between each layer of both samples was about 3 minutes which was spent for height measurement and system preparations for the next layer.

## 5.3 Results and Discussions

### 5.3.1 Preliminary Experiments

Figure 39 represents one of several examples that demonstrates the issues resulted from the misalignment of the wire and the arc. Despite the non-uniform beads, the adjustment of the plasma torch and the wire nozzle have arranged the blubs to be more aligned as small adjustments were applied.



**Figure 39: 3 beads with identical printing parameters (Current=25 A, Travel Speed = 100 mm/min, Wire Feed rate = 210 mm/min). The effect of wire and arc alignment can be visualized from top to bottom.**

Meanwhile, presence of the spherical deposited filler metal is believed to have been caused by the high heat density of the plasma arc and oxidation. The wire rapidly melted as it entered the plasma region, and the heat continues to melt the portion of the wire that is not inside the arc. The wire became misaligned as molten material formed a droplet attached to the wire, resulting in bending of the heated (hence softened) wire. The droplets fell on

the substrate due to gravity, and the process repeated itself. A solution was proposed to increase the wire feed rate to ensure the wire reaches the weld pool before fully melting. It was found that a wire feed rate more than 270 mm/min would cause collision with the substrate and a deflection of the wire, specially from the arc coming out of the 1 mm plasma nozzle. Figure 40 presents the 4 beads with similar welding parameters printed more than 30 minutes apart to ensure similar initial condition in terms of the substrate temperature. The variation of these beads is such that the conventional printing method could not be utilized with the current setup. Increasing the heat input and wire feed rate would potentially solve this issue, however, the thickness of the walls will increase beyond the goals of this research.



**Figure 40: The beads printed with the conventional printing method of similar printing parameters (10 mm of arc length, Current=28 A, Travel Speed = 90 mm/min, Wire Feed rate = 270 mm/min)**

### 5.3.2 Oxidation Analysis

After achieving an acceptable set of CHF parameters for the first layer (reported in Table 6), printing of subsequent layers yielded lack of bonding and misalignment of the deposits. Figure 41a shows the printed beads while Figure 41b is an example of the surface appearance of sample 1. The qualitative content of oxygen measured from different shades of grey is provided in Table 7. The comparison of the values indicates different levels of oxidation (e.g. the darker area is more oxidized compared to the lighter area).

**Table 7: Average oxygen content (%wt.) of the samples based on the shades of grey on the surface of the beads in Figure 41a detected by EDX.**

	Sample 1	Sample 2	Sample 3	Sample 4
Lightest (Spectrum 3)	1	2	2	1
Light Grey (Spectrum 2)	23	22	21	25
Grey (Spectrum 1)	36	37	43	42

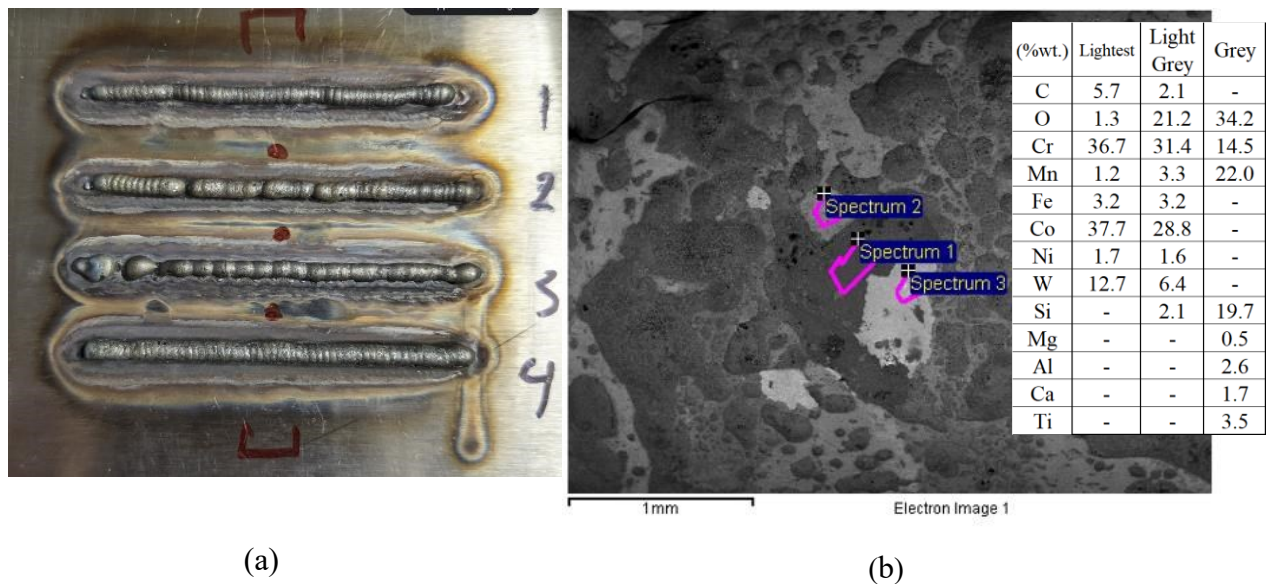


**Figure 41: a) Oxidation samples as described in Section 5.2.3. (b) An example of the shades of grey on Sample 1 along with the EDX results.**

The grey area is enriched in Mn and Cr as the light grey area is primarily Cr and Co. It was observed that lack of wetting due to oxidation prevents adhesion of subsequent layer, hence the resulted geometrical features. Xu et al. [110] had performed a similar study and confirmed that the oxide on the surface prevents desired wetting and spreading of the welding area. Additionally, they suggested that the oxide in a multilayer maraging steel wall move towards the top affecting the surface finish. This can be confirmed by the detection of Mn (Figure 41b) on top surface since the major source of Mn was in Stainless Steel 304 substrate.

### **5.3.3 CHF Specimens**

#### **5.3.3.1 Geometrical Features**

Figure 42 illustrates the two specimens where the average wall thicknesses are 3.30 mm and 3.40 mm for samples A and B, respectively. Even though the wire feed rate has increased by 29% compared to the GTAW-AM in Section 4.4.2, the average thickness increased by 5%, indicating the effects of narrower arc on the geometry of the beads. The average height of samples A and B was 9.80 mm and 10.00 mm, respectively. Compared to the CHF sample in GTAW-AM (Section 4.4.2), the average height of the samples A and B has increased by 32%. The measurements do not consider the corners. The geometrical features of both samples are similar, however, the second layer on sample A seems to have been shifted over the first layer (shown in Figure 42). The shifting could be due to high amount of oxidation on top surface of the first layer as it was printed with the highest

current. Also, it can be speculated that the longer melting time in sample B improves susceptibility of the final geometry to oxidation.

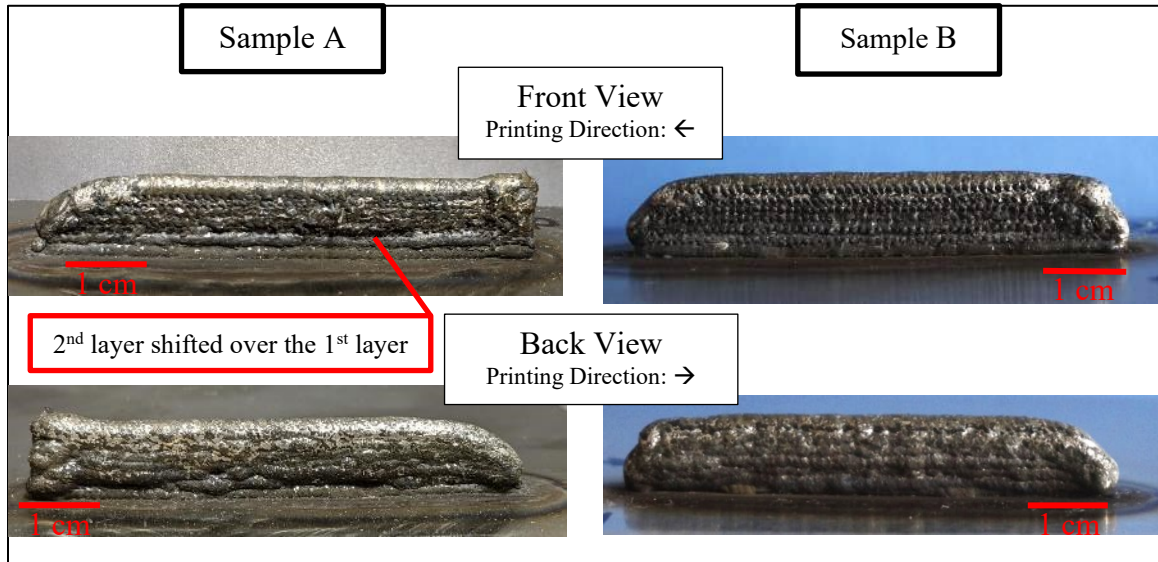
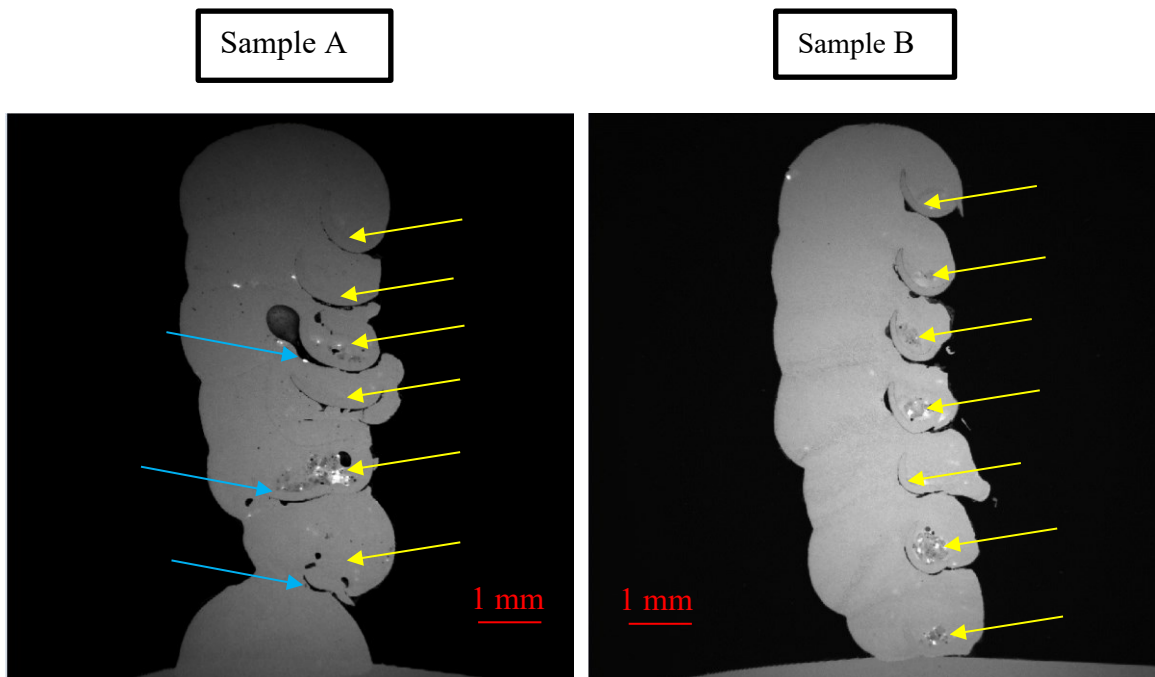


Figure 42: Images of the two printed samples at front and back view.

Furthermore, the uneven surface of the back side of the samples was discussed by Xu et al. [110] study. They showed that an inert environment produces more uniform beads. In addition to support an arc stability, a smooth (and clean) surface provides constant weld pool size and substrate for a uniform deposition. The presence of oxides on the surface of metal affects the energy density from the arc to the metal resulting in arc temperature variation due to the increased resistance of oxide (vs. metals), and hence local temperature increase on the surface [111]. Large amount of oxidation in samples A and B must be addressed by means of additional shielding gas. Researchers at Cranfield University have designed a shielding device which provides a laminar flow of argon gas over the substrate [112]. Such solutions can be utilized to prevent oxidation during PAW-AM.

### 5.3.3.2 Microstructural Analysis

Figure 43 provides the cross-sectional SEM images of both CHF samples. The presence of unmelted wire is evident in both samples. This occurred presumably due to the size of the arc being less than the wire diameter and the increased wire feed rate (to ensure the wire reaches the weld pool). Sample B does not show complete lack of adhesion between the layers. There is a relatively large crack between layer 1 and 2 for sample A due to oxidation. The longer heating time in sample B is a factor encouraging the formation of a more consistent weld pool.



**Figure 43: Overall cross-sectional SEM macrograph of the samples A and B. Yellow arrows indicate unmelted wire, and blue arrows indicate lack of bonding between layers. (Please note that lens distortion effect has caused the substrate arc)**

Figure 44 illustrates the microstructure of the 5<sup>th</sup> layer in both samples from a fully melted region. The microstructural features are similar in both samples, however, the size of the

microstructural constituents in the GTAW-AM sample were smaller than that from the PAW-AM due to lower energy density of GTAW.

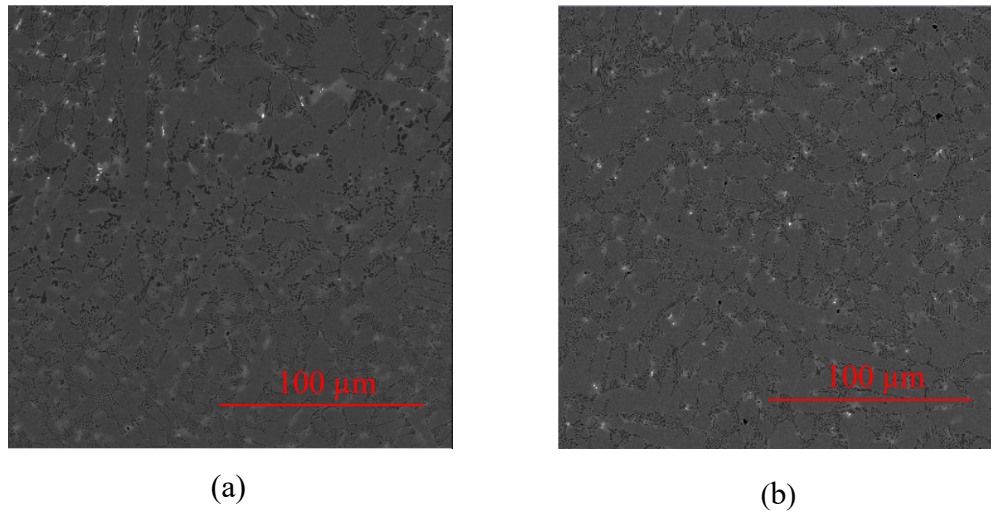


**Figure 44: SEM micrograph of a fully melted section towards the center of the 5th layer in a) Sample A and, b) Sample B.**

The defects presented in the samples, such as unmelted particles and insufficient interfacial bonding, determined that mechanical property evaluation was not necessary at this stage.

#### **5.4 Conclusion**

Plasma arc welding AM utilizes a high heat density but narrow power source for melting and depositing a wire layer-by-layer. It was considered that PAW-AM is capable of printing low thickness (<3.5 mm) walls from 1.2 mm Stellite 6 metal-cored wire. A 1 mm plasma nozzle was utilized for this purpose. The initial experiments with the conventional printing method indicated that the high heat density liquifies the wire before it reaches the weld pool and causing the formation of balls. As an alternative, the CHF method was utilized to produce two 7-layer samples, one having a longer high current duration (sample

B). Although the beads were deposited successively, the effects of oxidation prevented the complete bonding between layers. Both samples had the presence of unmelted wire within the microstructure. The sample with a larger high current duration did not show any lack of bonding which leads to the conclusion that longer heating of the surface reduces the effect of oxidation. The microstructural features in both samples were similar, however, coarser features were observed compared to the CHF sample in GTAW-AM.

## **Chapter 6: Conclusion and Future Work**

The focus of this thesis is on the additive manufacturing of low thickness (<3.5 mm) walls with metal-cored Stellite 6 wire and two welding methods. The challenge is to modify the GTAW and PAW processes commonly used for thicker walls. Preliminary experiments followed by the establishment of the parameters for each process were documented in this study. Macrostructure and microstructure analysis of the resulting samples were conducted to validate the effectiveness of the adopted parameters. The methods and procedures developed are summarized below.

### **6.1 Gas Tungsten Arc Welding Additive Manufacturing**

#### **6.1.1 Equipment Setup and Preliminary Experiments**

This research characterised nature of the wire and led to a reduced distance between the wire nozzle and the weld pool, as this distance promoted oscillation of the wire under the arc. Wire and arc misalignment associated with the wire oscillation affected the reliability of the deposited layers in a way that printing successive layers would not be possible. Critical calibration procedures minimized the misalignment problems. Furthermore, it was concluded that the conventional printing method produced unreliable beads in terms of geometry, repeatability, and the inability of printing successive layers.

#### **6.1.2 Coordinated Heat and Feed (CHF) Printing Strategy**

Upon realization of the disadvantages of the conventional printing method with the metal-cored wire, a novel method was developed: a CHF method, in which, independent of the travel speed, any amount of wire (as long as there is no setup related constraints) can be

melted where a path segment had just been heated. The CHF begins by creating a weld pool at a previously designated path segment and inserting the wire once the weld pool is at an ideal condition. After the wire insertion, the solidification of the deposit begins, usually accompanied by a lower heating parameter. The welding torch is moved to the next path segment and the same process is repeated until all path segments on the layer are completed.

### **6.1.3 CHF Validation**

The new method was validated by comparing a 7-layer CHF specimen with a 7-layer conventionally printed specimen. The macrostructural features in the CHF specimen were better in terms of surface roughness, interfacial defects and alignment between each successive layer. Both specimens had traces of unmelted wire towards their edges which would be removed during post AM process. Furthermore, the microstructures, hardness, and the dilution of the substrate into the printed metal were similar.

### **6.1.4 Future Work**

- New setup arrangements for the wire and arc positions should be studied to simplify multi-directional printing along with the prevention of wire deflection.
- The non-continuous nature of the CHF method should be studied to understand the underlining heat and mass transform and should also be actively controlled (by a feedback system) to prevent any non-compliances associated with the region between the bead segments such as residual stress and cracking.

- Decreasing the electrode size and studying the relationship among the electrode size and wall thickness and surface roughness.
- Numerical modeling of the conventional method and the CHF printing strategy shall be conducted to help understand the processes and enabling process improvements.
- Implementing a simple 3D laser scanner for preplanning the CHF wire feed rates to eliminate uneven surfaces.
- Establishing the appropriate CHF parameters and paths for corners, and fillets.

## **6.2 Plasma Arc Welding Additive Manufacturing**

This section is the preliminary research where the aim is to produce a low thickness wall using a plasma nozzle that is smaller than the wire diameter. This work is continuing by another researcher.

### **6.2.1 Equipment Setup and Preliminary Experiments**

The modification of the 3D printer control board was performed to interface the PAW system with the printer. Along with the manufacturing of the torch holder, a calibration process for alignment of the wire and arc was established. Furthermore, it was concluded that the conventional printing method could not be used to print cored wires due to high heat density of the arc, and lack of repeatability. Moreover, severe surface oxidation of some samples (including CHF and conventional) was observed. The amount of oxidation on the surface prevents the formation of a uniform weld pool as the successive layer is deposited.

### **6.2.2 CHF Printing Strategy**

Seen that the conventional method was not suitable for cored wires, two 7-layer CHF walls were printed. The amount of time for creating the weld pool in sample A was less than sample B. The surface finish was rougher than CHF GTAW-AM samples due to oxidation. Both samples showed relatively similar geometrical features. Even though the wire feed rate increased by 29%, the average thickness of the samples only augmented by 6%. This is an indication that the selection of PAW system is appropriate to achieve the goals of printing thin wall. In the microstructural analysis of the samples, the sample B with more stable weld pool did not have an indication of the lack of bonding, whereas this defect was evident in the other sample A. Both samples were not selected for further study as all layers contained amount of unmelted wire.

### **6.2.3 Future Work**

- Process modification to prevent oxidation.
- Redesign of the torch and wire holders for improved alignment accuracy and the ability to print at low arc lengths.
- Utilization of a modified CHF printing strategy in a way that the torch is lowered during the solidification to provide more shielding gas.

## References

- [1] W. E. Frazier, “Metal Additive Manufacturing: A Review,” *Journal of Materials Engineering and Performance*, vol. 23, no. 6, pp. 1917–1928, Jun. 2014, doi: 10.1007/s11665-014-0958-z.
- [2] M. Kumke, H. Watschke, and T. Vietor, “A new methodological framework for design for additive manufacturing,” *Virtual and Physical Prototyping*, vol. 11, no. 1, pp. 3–19, Jan. 2016, doi: 10.1080/17452759.2016.1139377.
- [3] D. L. Bourell, “Perspectives on Additive Manufacturing,” *Annual Review of Materials Research*, vol. 46, no. 1, pp. 1–18, Jul. 2016, doi: 10.1146/annurev-matsci-070115-031606.
- [4] J. Bonnín Roca, P. Vaishnav, E. R. H. Fuchs, and M. G. Morgan, “Policy needed for additive manufacturing,” *Nature Materials*, vol. 15, no. 8, pp. 815–818, Aug. 2016, doi: 10.1038/nmat4658.
- [5] “About Réseau Québec-3D - Réseau Québec-3D.” <https://www.reseauquebec3d.com/en/about-reseau-quebec-3d> (accessed Sep. 19, 2021).
- [6] “FedDev Ontario invests in Waterloo-based additive manufacturing consortium - Canada.ca.” <https://www.canada.ca/en/economic-development-southern-ontario/news/2021/07/feddev-ontario-invests-in-waterloo-based-additive-manufacturing-consortium.html> (accessed Sep. 19, 2021).

- [7] B. Blakey-Milner *et al.*, “Metal additive manufacturing in aerospace: A review,” *Materials & Design*, vol. 209, p. 110008, Nov. 2021, doi: 10.1016/j.matdes.2021.110008.
- [8] F. Mouriaux and A. Berkau, “Certified for Universal Success: Additive Manufacturing of Satellite Components,” 2016. Accessed: Sep. 20, 2021. [Online]. Available: [www.citim.de](http://www.citim.de)
- [9] H. A. Eschenauer and N. Olhoff, “Topology optimization of continuum structures: A review\*,” *Applied Mechanics Reviews*, vol. 54, no. 4, pp. 331–390, Jul. 2001, doi: 10.1115/1.1388075.
- [10] GE Additive, “OUR JOURNEY.” Accessed: Sep. 20, 2021. [Online]. Available: <https://www.ge.com/additive/sites/default/files/2020-08/GE9X%20Additive%20parts.pdf>
- [11] L. E. Murr, “Additive manufacturing of biomedical devices: an overview,” *Materials Technology*, vol. 33, no. 1, pp. 57–70, Jan. 2018, doi: 10.1080/10667857.2017.1389052.
- [12] S. L. Sing, J. An, W. Y. Yeong, and F. E. Wiria, “Laser and electron-beam powder-bed additive manufacturing of metallic implants: A review on processes, materials and designs,” *Journal of Orthopaedic Research*, vol. 34, no. 3, pp. 369–385, Mar. 2016, doi: 10.1002/jor.23075.
- [13] Y. Katsuura and S. A. Qureshi, “Additive Manufacturing for Metal Applications in Orthopaedic Surgery,” *Journal of the American Academy of Orthopaedic Surgeons*, vol. 28, no. 8, pp. e349–e355, Apr. 2020, doi: 10.5435/JAAOS-D-19-00420.

- [14] “Cervical Spondylotic Myelopathy (CSM) - Spinal Cord Compression - OrthoInfo - AAOS.” <https://orthoinfo.aaos.org/en/diseases--conditions/cervical-spondylotic-myelopathy-spinal-cord-compression/> (accessed Sep. 22, 2021).
- [15] “The Use of Titanium Mesh Cages in the Cervical Spine : Clinical Orthopaedics and Related Research®.” [https://journals.lww.com/clinorthop/Fulltext/2002/01000/The\\_Use\\_of\\_Titanium\\_Mesh\\_Cages\\_in\\_the\\_Cervical.6.aspx](https://journals.lww.com/clinorthop/Fulltext/2002/01000/The_Use_of_Titanium_Mesh_Cages_in_the_Cervical.6.aspx) (accessed Sep. 22, 2021).
- [16] “IOS Hospital | Glossary of Terms | Northwest Ohio Orthopedic Surgery.” <https://www.ioshospital.com/orthopaedics/learnMore/glossaryOfTerms.aspx> (accessed Oct. 26, 2021).
- [17] T. Lu *et al.*, “Single-Level Anterior Cervical Corpectomy and Fusion Using a New 3D-Printed Anatomy-Adaptive Titanium Mesh Cage for Treatment of Cervical Spondylotic Myelopathy and Ossification of the Posterior Longitudinal Ligament: A Retrospective Case Series Study.,” *Medical science monitor : international medical journal of experimental and clinical research*, vol. 23, pp. 3105–3114, Jun. 2017, doi: 10.12659/msm.901993.
- [18] Y. Wang, R. Blache, and X. Xu, “Selection of additive manufacturing processes,” *Rapid Prototyping Journal*, vol. 23, no. 2, pp. 434–447, Mar. 2017, doi: 10.1108/RPJ-09-2015-0123.
- [19] X. Yao, S. K. Moon, and G. Bi, “A Cost-Driven Design Methodology for Additive Manufactured Variable Platforms in Product Families,” *Journal of Mechanical Design*, vol. 138, no. 4, Apr. 2016, doi: 10.1115/1.4032504.

- [20] S. Yim and D. Rosen, “Build Time and Cost Models for Additive Manufacturing Process Selection,” in *Volume 2: 32nd Computers and Information in Engineering Conference, Parts A and B*, Aug. 2012, vol. 2, no. PARTS A AND B, pp. 375–382. doi: 10.1115/DETC2012-70940.
- [21] J. Ding, M. Baumers, E. A. Clark, and R. D. Wildman, “The economics of additive manufacturing: Towards a general cost model including process failure,” *International Journal of Production Economics*, vol. 237, p. 108087, Jul. 2021, doi: 10.1016/j.ijpe.2021.108087.
- [22] P. Alexander, S. Allen, and D. Dutta, “Part orientation and build cost determination in layered manufacturing,” *Computer-Aided Design*, vol. 30, no. 5, pp. 343–358, 1998.
- [23] B. Dutta and F. H. (Sam) Froes, “The Additive Manufacturing (AM) of titanium alloys,” *Metal Powder Report*, vol. 72, no. 2, pp. 96–106, Mar. 2017, doi: 10.1016/j.mprp.2016.12.062.
- [24] S. L. Sing, J. An, W. Y. Yeong, and F. E. Wiria, “Laser and electron-beam powder-bed additive manufacturing of metallic implants: A review on processes, materials and designs,” *Journal of Orthopaedic Research*, vol. 34, no. 3, pp. 369–385, Mar. 2016, doi: 10.1002/jor.23075.
- [25] L. Thijs, F. Verhaeghe, T. Craeghs, J. van Humbeeck, and J.-P. Kruth, “A study of the microstructural evolution during selective laser melting of Ti–6Al–4V,” *Acta Materialia*, vol. 58, no. 9, pp. 3303–3312, May 2010, doi: 10.1016/j.actamat.2010.02.004.

- [26] P. Hanzl, M. Zetek, T. Bakša, and T. Kroupa, “The Influence of Processing Parameters on the Mechanical Properties of SLM Parts,” *Procedia Engineering*, vol. 100, no. January, pp. 1405–1413, Jan. 2015, doi: 10.1016/j.proeng.2015.01.510.
- [27] J. Kruth, P. Mercelis, J. van Vaerenbergh, L. Froyen, and M. Rombouts, “Binding mechanisms in selective laser sintering and selective laser melting,” *Rapid Prototyping Journal*, vol. 11, no. 1, pp. 26–36, Feb. 2005, doi: 10.1108/13552540510573365.
- [28] E. Yasa, K. Kellens, W. Dewulf, and J. R. Duflou, “Environmental assessment of selective laser melting and selective laser sintering,” 2010, Accessed: Nov. 02, 2021. [Online]. Available: <https://www.researchgate.net/publication/266450713>
- [29] A. Röttger *et al.*, “Microstructure and mechanical properties of 316L austenitic stainless steel processed by different SLM devices,” *The International Journal of Advanced Manufacturing Technology*, vol. 108, no. 3, pp. 769–783, May 2020, doi: 10.1007/s00170-020-05371-1.
- [30] J. Parthasarathy, B. Starly, S. Raman, and A. Christensen, “Mechanical evaluation of porous titanium (Ti6Al4V) structures with electron beam melting (EBM),” *Journal of the Mechanical Behavior of Biomedical Materials*, vol. 3, no. 3, pp. 249–259, Apr. 2010, doi: 10.1016/j.jmbbm.2009.10.006.
- [31] L. Cordova, M. Campos, and T. Tinga, “Revealing the Effects of Powder Reuse for Selective Laser Melting by Powder Characterization,” *JOM*, vol. 71, no. 3, pp. 1062–1072, Mar. 2019, doi: 10.1007/s11837-018-3305-2.

- [32] E. Schlienger *et al.*, “Near Net Shape production of metal components using LENS,” Jul. 1998. Accessed: Oct. 03, 2021. [Online]. Available: <https://www-osti-gov.proxy.library.carleton.ca/biblio/650377>
- [33] S. M. Thompson, L. Bian, N. Shamsaei, and A. Yadollahi, “An overview of Direct Laser Deposition for additive manufacturing; Part I: Transport phenomena, modeling and diagnostics,” *Additive Manufacturing*, vol. 8, pp. 36–62, Oct. 2015, doi: 10.1016/j.addma.2015.07.001.
- [34] K. Hofer, A. Haelsig, and P. Mayr, “Arc-based additive manufacturing of steel components—comparison of wire- and powder-based variants,” *Welding in the World*, vol. 62, no. 2, pp. 243–247, Mar. 2018, doi: 10.1007/s40194-017-0527-9.
- [35] S. W. Williams, F. Martina, A. C. Addison, J. Ding, G. Pardal, and P. Colegrove, “Wire + Arc Additive Manufacturing,” *Materials Science and Technology*, vol. 32, no. 7, pp. 641–647, May 2016, doi: 10.1179/1743284715Y.0000000073.
- [36] C. Xia *et al.*, “A review on wire arc additive manufacturing: Monitoring, control and a framework of automated system,” *Journal of Manufacturing Systems*, vol. 57, pp. 31–45, Oct. 2020, doi: 10.1016/j.jmsy.2020.08.008.
- [37] S. Pattanayak and S. K. Sahoo, “Gas metal arc welding based additive manufacturing—a review,” *CIRP Journal of Manufacturing Science and Technology*, vol. 33, pp. 398–442, May 2021, doi: 10.1016/j.cirpj.2021.04.010.
- [38] B. Cong, Z. Qi, B. Qi, H. Sun, G. Zhao, and J. Ding, “A Comparative Study of Additively Manufactured Thin Wall and Block Structure with Al-6.3%Cu Alloy Using Cold Metal Transfer Process,” *Applied Sciences*, vol. 7, no. 3, p. 275, Mar. 2017, doi: 10.3390/app7030275.

- [39] P. Kazanas, P. Deherkar, P. Almeida, H. Lockett, and S. Williams, “Fabrication of geometrical features using wire and arc additive manufacture,” *Proceedings of the Institution of Mechanical Engineers, Part B: Journal of Engineering Manufacture*, vol. 226, no. 6, pp. 1042–1051, Jun. 2012, doi: 10.1177/0954405412437126.
- [40] K. Somlo and G. Sziebig, “Aspects of Multi-pass GTAW of Low Alloyed Steels,” *IFAC-PapersOnLine*, vol. 52, no. 22, pp. 101–107, Jan. 2019, doi: 10.1016/j.ifacol.2019.11.056.
- [41] C. Shen, Z. Pan, D. Cuiuri, D. Ding, and H. Li, “Influences of deposition current and interpass temperature to the Fe<sub>3</sub>Al-based iron aluminide fabricated using wire-arc additive manufacturing process,” *International Journal of Advanced Manufacturing Technology*, vol. 88, no. 5–8, pp. 2009–2018, 2017, doi: 10.1007/s00170-016-8935-3.
- [42] M. Dinovitzer, X. Chen, J. Laliberte, X. Huang, and H. Frei, “Effect of wire and arc additive manufacturing (WAAM) process parameters on bead geometry and microstructure,” *Additive Manufacturing*, vol. 26, pp. 138–146, Mar. 2019, doi: 10.1016/j.addma.2018.12.013.
- [43] A. Aibe, K. Nomura, and S. Asai, “Tomographic measurement of current density and heat input density for tilting TIG arc,” <https://doi-org.proxy.library.carleton.ca/10.1080/09507116.2020.1866360>, vol. 33, no. 10–12, pp. 438–449, 2021, doi: 10.1080/09507116.2020.1866360.
- [44] C. S. Wu, L. Wang, W. J. Ren, and X. Y. Zhang, “Plasma arc welding: Process, sensing, control and modeling,” *Journal of Manufacturing Processes*, vol. 16, no. 1, pp. 74–85, 2014, doi: 10.1016/j.jmapro.2013.06.004.

- [45] Z. M. Liu, S. Cui, Z. Luo, C. Zhang, Z. Wang, and Y. Zhang, "Plasma arc welding: Process variants and its recent developments of sensing, controlling and modeling," *Journal of Manufacturing Processes*, vol. 23, pp. 315–327, 2016, doi: 10.1016/j.jmapro.2016.04.004.
- [46] R. Zhang, F. Jiang, and S. Chen, "Comparison of energy acted on workpiece among Twin-body Plasma Arc Welding, Non-transferred Plasma Arc Welding and Plasma Arc Welding," *Journal of Manufacturing Processes*, vol. 24, pp. 152–160, 2016, doi: 10.1016/j.jmapro.2016.08.009.
- [47] B. Wu *et al.*, "A review of the wire arc additive manufacturing of metals: properties, defects and quality improvement," *Journal of Manufacturing Processes*, vol. 35. Elsevier Ltd, pp. 127–139, Oct. 01, 2018. doi: 10.1016/j.jmapro.2018.08.001.
- [48] T. D. Ngo, A. Kashani, G. Imbalzano, K. T. Q. Nguyen, and D. Hui, "Additive manufacturing (3D printing): A review of materials, methods, applications and challenges," *Composites Part B: Engineering*, vol. 143, pp. 172–196, Jun. 2018, doi: 10.1016/J.COMPOSITESB.2018.02.012.
- [49] N. Shamsaei, A. Yadollahi, L. Bian, and S. M. Thompson, "An overview of Direct Laser Deposition for additive manufacturing; Part II: Mechanical behavior, process parameter optimization and control," *Additive Manufacturing*, vol. 8, pp. 12–35, 2015, doi: 10.1016/j.addma.2015.07.002.
- [50] S. Sahoo, A. Joshi, V. K. Balla, M. Das, and S. Roy, "Site-specific microstructure, porosity and mechanical properties of LENS<sup>TM</sup> processed Ti-6Al-4V alloy,"

- Materials Science and Engineering: A*, vol. 820, p. 141494, 2021, doi:  
10.1016/j.msea.2021.141494.
- [51] T. J. Carter, “Common failures in gas turbine blades,” 2004, doi:  
10.1016/j.engfailanal.2004.07.004.
- [52] R. Shoja-Razavi, “Laser Surface Treatment of Stellite 6 Coating Deposited by HVOF on 316L Alloy,” *Journal of Materials Engineering and Performance*, vol. 25, doi: 10.1007/s11665-016-2138-9.
- [53] Z. Li *et al.*, “Characterization of microstructure and mechanical properties of stellite 6 part fabricated by wire arc additive manufacturing,” *Metals*, vol. 9, no. 4, p. 474, Apr. 2019, doi: 10.3390/met9040474.
- [54] B. Berman, “3-D printing: The new industrial revolution,” *Business Horizons*, vol. 55, no. 2, pp. 155–162, Mar. 2012, doi: 10.1016/j.bushor.2011.11.003.
- [55] C. Buchanan and L. Gardner, “Metal 3D printing in construction: A review of methods, research, applications, opportunities and challenges,” *Engineering Structures*, vol. 180, pp. 332–348, Feb. 2019, doi:  
10.1016/j.engstruct.2018.11.045.
- [56] M. K. Thompson *et al.*, “Design for Additive Manufacturing: Trends, opportunities, considerations, and constraints,” *CIRP Annals*, vol. 65, no. 2, pp. 737–760, Jan. 2016, doi: 10.1016/j.cirp.2016.05.004.
- [57] J. W. Stansbury and M. J. Idacavage, “3D printing with polymers: Challenges among expanding options and opportunities,” *Dental Materials*, vol. 32, no. 1, pp. 54–64, Jan. 2016, doi: 10.1016/J.DENTAL.2015.09.018.

- [58] “Layer by Layer | MIT Technology Review.”  
<https://www.technologyreview.com/2011/12/19/20869/layer-by-layer/> (accessed Sep. 08, 2021).
- [59] “An Epiphany Of Disruption: GE Additive Chief Explains How 3D Printing Will Upend Manufacturing | GE News.” <https://www.ge.com/news/reports/epiphany-disruption-ge-additive-chief-explains-3d-printing-will-upend-manufacturing> (accessed Sep. 09, 2021).
- [60] Y. Hu, W. Cong, X. Wang, Y. Li, F. Ning, and H. Wang, “Laser deposition-additive manufacturing of TiB-Ti composites with novel three-dimensional quasi-continuous network microstructure: Effects on strengthening and toughening,” *Composites Part B: Engineering*, vol. 133, pp. 91–100, Jan. 2018, doi: 10.1016/J.COMPOSITESB.2017.09.019.
- [61] E. Sheydaeian and E. Toyserkani, “A new approach for fabrication of titanium-titanium boride periodic composite via additive manufacturing and pressure-less sintering,” *Composites Part B: Engineering*, vol. 138, pp. 140–148, Apr. 2018, doi: 10.1016/J.COMPOSITESB.2017.11.035.
- [62] D. Herzog, V. Seyda, E. Wycisk, and C. Emmelmann, “Additive manufacturing of metals,” *Acta Materialia*, vol. 117, pp. 371–392, Sep. 2016, doi: 10.1016/J.ACTAMAT.2016.07.019.
- [63] K. S. Chan, M. Koike, R. L. Mason, and T. Okabe, “Fatigue Life of Titanium Alloys Fabricated by Additive Layer Manufacturing Techniques for Dental Implants,” *Metallurgical and Materials Transactions A 2012 44:2*, vol. 44, no. 2, pp. 1010–1022, Oct. 2012, doi: 10.1007/S11661-012-1470-4.

- [64] W. E. Frazier, “Direct Digital Manufacturing of Metallic Components: Vision and Roadmap”.
- [65] J. A. Scott, “Additive Manufacturing: Status and Opportunities,” 2012, Accessed: Aug. 10, 2021. [Online]. Available: <https://www.researchgate.net/publication/312153354>
- [66] B. E. Carroll, T. A. Palmer, and A. M. Beese, “Anisotropic tensile behavior of Ti-6Al-4V components fabricated with directed energy deposition additive manufacturing,” *Acta Materialia*, vol. 87, pp. 309–320, 2015, doi: 10.1016/j.actamat.2014.12.054.
- [67] C. Li *et al.*, “Effects of magnesium on the microstructure and properties of Al–Si alloy deposited by wire and arc-based additive manufacturing,” *Materials Technology*, vol. 36, no. 13, pp. 793–798, 2021, doi: 10.1080/10667857.2020.1797284/FORMAT/EPUB.
- [68] James B. C. Wu; Volker Hellinger; Matthew X. Yao, “Weldable, crack-resistant Co-based alloy and overlay,” US8603264B2, May 30, 2013
- [69] M. Dinovitzer, “Development and Characterization of Additive Manufacturing of Superalloy Hastelloy X Using a Cost Effective TIG Technique,” 2020.
- [70] X. Wang, A. Wang, and Y. Li, “Study on the deposition accuracy of omnidirectional GTAW-based additive manufacturing,” *Journal of Materials Processing Technology*, vol. 282, p. 116649, Aug. 2020, doi: 10.1016/j.jmatprotec.2020.116649.

- [71] J. Qiao, C. Wu, and Y. Li, "Numerical Analysis of Keyhole and Weld Pool Behaviors in Ultrasonic-Assisted Plasma Arc Welding Process," *Materials* 2021, Vol. 14, Page 703, vol. 14, no. 3, p. 703, Feb. 2021, doi: 10.3390/MA14030703.
- [72] H. Matsui and T. Hattori, "Welding International Control of wire tip deflection in a consumable electrode type arc welding torch Control of wire tip deflection in a consumable electrode type arc welding torch Toyota Hlitor Corporation," *Selected from Quarterly Journal of Japan Welding Society*, vol. 13, no. 3, pp. 282–289, 1999, doi: 10.1080/09507119909447362.
- [73] Q. Zhan, Y. Liang, J. Ding, and S. Williams, "A wire deflection detection method based on image processing in wire + arc additive manufacturing," *The International Journal of Advanced Manufacturing Technology*, vol. 89, no. 1–4, pp. 755–763, Mar. 2017, doi: 10.1007/s00170-016-9106-2.
- [74] R. C. Hibbeler, *Mechanics of materials*. Singapore: Prentice Hall, 2014.
- [75] "smoothieboard [Smoothieware]." <https://smoothieware.org/smoothieboard> (accessed Nov. 03, 2021).
- [76] "Duet 2 WiFi/Ethernet Hardware Overview - Duet3D." [https://duet3d.dozuki.com/Wiki/Hardware\\_Overview](https://duet3d.dozuki.com/Wiki/Hardware_Overview) (accessed Nov. 03, 2021).
- [77] "Duex 2 and Duex 5 - Duet3D." [https://duet3d.dozuki.com/Wiki/Duex2\\_and\\_Duex5\\_Features](https://duet3d.dozuki.com/Wiki/Duex2_and_Duex5_Features) (accessed Nov. 03, 2021).
- [78] Deepika and N. Yadav, "Design of Dual Master I2C Bus Controller and Interfacing it with DC Motor," *Proceedings - IEEE 2018 International Conference*

*on Advances in Computing, Communication Control and Networking, ICACCCN 2018*, pp. 668–673, Oct. 2018, doi: 10.1109/ICACCCN.2018.8748677.

- [79] C. K. Chua, C. H. Wong, and W. Y. Yeong, “Introduction to 3D Printing or Additive Manufacturing,” in *Standards, Quality Control, and Measurement Sciences in 3D Printing and Additive Manufacturing*, Elsevier, 2017, pp. 1–29. doi: 10.1016/b978-0-12-813489-4.00001-5.
- [80] D. Ding, Z. Pan, D. Cuiuri, and H. Li, “Wire-feed additive manufacturing of metal components: technologies, developments and future interests,” *International Journal of Advanced Manufacturing Technology*, vol. 81, no. 1–4. pp. 465–481, 2015. doi: 10.1007/s00170-015-7077-3.
- [81] A. Busachi, J. Erkoyuncu, P. Colegrove, F. Martina, and J. Ding, “Designing a WAAM based manufacturing system for defence applications,” in *Procedia CIRP*, Jan. 2015, vol. 37, pp. 48–53. doi: 10.1016/j.procir.2015.08.085.
- [82] P. Kazanas, P. Deherkar, P. Almeida, H. Lockett, and S. Williams, “Fabrication of geometrical features using wire and arc additive manufacture,” *Proceedings of the Institution of Mechanical Engineers, Part B: Journal of Engineering Manufacture*, vol. 226, no. 6, pp. 1042–1051, Jun. 2012, doi: 10.1177/0954405412437126.
- [83] J. S. Panchagnula and S. Simhambhatla, “Manufacture of complex thin-walled metallic objects using weld-deposition based additive manufacturing,” *Robotics and Computer-Integrated Manufacturing*, vol. 49, pp. 194–203, 2018, doi: 10.1016/j.rcim.2017.06.003.
- [84] Z. Lin, C. Goulas, W. Ya, and M. J. M. Hermans, “Microstructure and mechanical properties of medium carbon steel deposits obtained via wire and arc additive

- manufacturing using metal-cored wire,” *Metals*, vol. 9, no. 6, p. 673, Jun. 2019, doi: 10.3390/met9060673.
- [85] Z. Lin *et al.*, “Deposition of Stellite 6 alloy on steel substrates using wire and arc additive manufacturing,” *International Journal of Advanced Manufacturing Technology*, vol. 111, no. 1, pp. 411–426, Sep. 2020, doi: 10.1007/s00170-020-06116-w.
- [86] L. Wang, J. Xue, and Q. Wang, “Correlation between arc mode, microstructure, and mechanical properties during wire arc additive manufacturing of 316L stainless steel,” *Materials Science and Engineering: A*, vol. 751, pp. 183–190, 2019, doi: 10.1016/j.msea.2019.02.078.
- [87] G. P. Rajeev, M. R. Rahul, M. Kamaraj, and S. R. Bakshi, “Microstructure and high temperature mechanical properties of wire arc additively deposited Stellite 6 alloy,” *Materialia*, vol. 12, p. 100724, 2020, doi: 10.1016/j.mtla.2020.100724.
- [88] Z. Li *et al.*, “Reducing arc heat input and obtaining equiaxed grains by hot-wire method during arc additive manufacturing titanium alloy,” *Materials Science and Engineering A*, vol. 742, pp. 287–294, Jan. 2019, doi: 10.1016/j.msea.2018.11.022.
- [89] Q. Wu *et al.*, “Obtaining uniform deposition with variable wire feeding direction during wire-feed additive manufacturing,” *Materials and Manufacturing Processes*, vol. 32, no. 16, pp. 1881–1886, 2017, doi: 10.1080/10426914.2017.1364860.
- [90] T. Xu, S. Tang, C. Liu, Z. Li, H. Fan, and S. Y. Ma, “Obtaining large-size pyramidal lattice cell structures by pulse wire arc additive manufacturing,”

*Materials and Design*, vol. 187, p. 108401, 2020, doi:  
10.1016/j.matdes.2019.108401.

- [91] B. Wu *et al.*, “Effects of heat accumulation on the arc characteristics and metal transfer behavior in Wire Arc Additive Manufacturing of Ti6Al4V,” *Journal of Materials Processing Technology*, vol. 250, pp. 304–312, 2017, doi:  
10.1016/j.jmatprotec.2017.07.037.
- [92] G. Marinelli, F. Martina, S. Ganguly, and S. Williams, “Development of Wire + Arc additive manufacture for the production of large-scale unalloyed tungsten components,” *International Journal of Refractory Metals and Hard Materials*, vol. 82, pp. 329–335, 2019, doi: 10.1016/j.ijrmhm.2019.05.009.
- [93] N. Rodriguez, L. Vázquez, I. Huarte, E. Arruti, I. Taberero, and P. Alvarez, “Wire and arc additive manufacturing: a comparison between CMT and TopTIG processes applied to stainless steel,” *Welding in the World*, vol. 62, no. 5, pp. 1083–1096, 2018, doi: 10.1007/s40194-018-0606-6.
- [94] G. Posch, K. Chladil, and H. Chladil, “Material properties of CMT—metal additive manufactured duplex stainless steel blade-like geometries,” *Welding in the World*, vol. 61, no. 5, pp. 873–882, Sep. 2017, doi: 10.1007/s40194-017-0474-5.
- [95] A. Mathivanan, A. Senthilkumar, and K. Devakumaran, “Pulsed current and dual pulse gas metal arc welding of grade AISI: 310S austenitic stainless steel,” *Defence Technology*, vol. 11, no. 3, pp. 269–274, Sep. 2015, doi:  
10.1016/j.dt.2015.05.006.
- [96] Q. Wu, Z. Ma, G. Chen, C. Liu, D. Ma, and S. Ma, “Obtaining fine microstructure and unsupported overhangs by low heat input pulse arc additive manufacturing,”

- Journal of Manufacturing Processes*, vol. 27, no. June, pp. 198–206, 2017, doi: 10.1016/j.jmapro.2017.05.004.
- [97] M. Yao, “Tubular Wires - An Overview,” Belleville, ON, Canada, 2020.
- [98] Kennametal, “Stellite Alloys [Brochure],” *Stellite alloys At a glance*. 2018.  
Accessed: Jan. 19, 2020. [Online]. Available:  
[https://www.kennametal.com/content/dam/kennametal/kennametal/common/Resources/Catalogs-Literature/Stellite/B-18-05784\\_KMT\\_Stellite\\_JetKote\\_Brochure.pdf](https://www.kennametal.com/content/dam/kennametal/kennametal/common/Resources/Catalogs-Literature/Stellite/B-18-05784_KMT_Stellite_JetKote_Brochure.pdf)
- [99] B. Baufeld, O. Van der Biest, and R. Gault, “Additive manufacturing of Ti-6Al-4V components by shaped metal deposition: Microstructure and mechanical properties,” *Materials and Design*, vol. 31, no. SUPPL. 1, pp. S106–S111, 2010, doi: 10.1016/j.matdes.2009.11.032.
- [100] B. Wu, Z. Pan, D. Ding, D. Cuiuri, and H. Li, “Effects of heat accumulation on microstructure and mechanical properties of Ti6Al4V alloy deposited by wire arc additive manufacturing,” *Additive Manufacturing*, vol. 23, pp. 151–160, Oct. 2018, doi: 10.1016/j.addma.2018.08.004.
- [101] S. Ríos, P. A. Colegrove, F. Martina, and S. W. Williams, “Analytical process model for wire + arc additive manufacturing,” *Additive Manufacturing*, vol. 21, pp. 651–657, May 2018, doi: 10.1016/j.addma.2018.04.003.
- [102] M. Jou, “Experimental Study and Modeling of GTA Welding Process,” *Journal of Manufacturing Science and Engineering*, vol. 125, no. 4, pp. 801–808, Nov. 2003, doi: 10.1115/1.1537740.

- [103] M. Wilson, "TIP TIG: new technology for welding," *Industrial Robot: An International Journal*, vol. 34, no. 6, pp. 462–466, Oct. 2007, doi: 10.1108/01439910710832057.
- [104] R. H. Gonçalves e Silva, K. Correa Riffel, M. Pompermaier Okuyama, and G. Dalpiaz, "Effect of dynamic wire in the GTAW process," *Journal of Materials Processing Technology*, vol. 269, pp. 91–101, Jul. 2019, doi: 10.1016/j.jmatprotec.2019.01.033.
- [105] P. A. Kobryn, E. H. Moore, and S. L. Semiatin, "THE EFFECT OF LASER POWER AND TRAVERSE SPEED ON MICROSTRUCTURE, POROSITY, AND BUILD HEIGHT IN LASER-DEPOSITED Ti-6Al-4V." Accessed: Oct. 24, 2020. [Online]. Available: [www.elsevier.com/locate/scriptamat](http://www.elsevier.com/locate/scriptamat)
- [106] J. F. Lancaster, "The physics of welding," *Physics in Technology*, vol. 15, no. 2, pp. 73–79, Mar. 1984, doi: 10.1088/0305-4624/15/2/I05.
- [107] N. A. Rosli, M. R. Alkahari, M. F. bin Abdollah, S. Maidin, F. R. Ramli, and S. G. Herawan, "Review on effect of heat input for wire arc additive manufacturing process," *Journal of Materials Research and Technology*, vol. 11, pp. 2127–2145, Mar. 2021, doi: 10.1016/j.jmrt.2021.02.002.
- [108] C. Wang, W. Suder, J. Ding, and S. Williams, "The effect of wire size on high deposition rate wire and plasma arc additive manufacture of Ti-6Al-4V," *Journal of Materials Processing Technology*, vol. 288, p. 116842, Feb. 2021, doi: 10.1016/j.jmatprotec.2020.116842.
- [109] F. Martina, J. Mehnen, S. W. Williams, P. Colegrove, and F. Wang, "Investigation of the benefits of plasma deposition for the additive layer manufacture of Ti-6Al-

- 4V,” *Journal of Materials Processing Technology*, vol. 212, no. 6, pp. 1377–1386, Jun. 2012, doi: 10.1016/j.jmatprotec.2012.02.002.
- [110] X. Xu, J. Ding, S. Ganguly, C. Diao, and S. Williams, “Oxide accumulation effects on wire + arc layer-by-layer additive manufacture process,” *Journal of Materials Processing Technology*, vol. 252, pp. 739–750, 2017, doi: 10.1016/j.jmatprotec.2017.10.030.
- [111] S. Leconte, P. Paillard, P. Chapelle, G. Henrion, and J. Saindrenan, “Science and Technology of Welding and Joining Effect of oxide fluxes on activation mechanisms of tungsten inert gas process Effect of oxide fluxes on activation mechanisms of tungsten inert gas process,” *Science and Technology of Welding and Joining*, vol. 11, no. 4, pp. 389–397, Jul. 2006, doi: 10.1179/174329306X129544.
- [112] J. Ding, P. Colegrove, F. Martina, S. Williams, R. Wiktorowicz, and M. R. Palt, “Development of a laminar flow local shielding device for wire + arc additive manufacture,” *Journal of Materials Processing Technology*, vol. 226, pp. 99–105, 2015, doi: 10.1016/j.jmatprotec.2015.07.005.

## Appendix A - Failed Square Printing

This section provides the results for failed attempts in printing a square with the GTAW-AM. The printing parameter has been similar to the parameter reported in Chapter 4, however, the main trial and error process has been done on the edges of the squares where the printing direction changes. The main idea has been to rotate the weld pool in a way that the larger ellipse (in a double ellipsoidal heat source model) is colinear with the new travel direction. Also, it is necessary to prevent any overlap that can cause a bump or a cavity. The first acceptable sample included 7 layers and the printing had begun from the corners of the square. Figure A 1 represents the path that was chosen for printing the specimen, the labels represent the order at which the beads were deposited. Beads 1 and 2 were printed consequently but the torch rapidly moved to the beginning of the bead 3 for the rest of the print process. The gaps were chosen to provide the best overlap for the most uniform bead. The 2 mm gap provided the best result as smaller gaps were not possible with the setup.

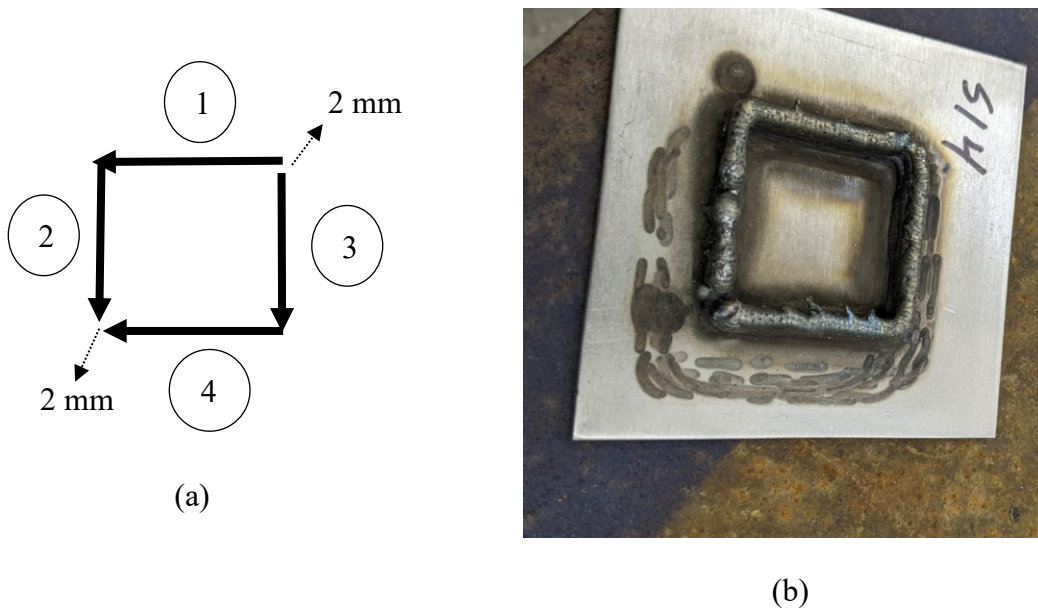


**Figure A 1: First acceptable square sample using the parameters reported in Chapter 4. a) The printing path and the appropriate gaps. b) The final printed specimen.**

As the setup could not be adjusted, it was decided to abandon the square printing and focus on the PAW process.